



Asymptotic study of linear instability in a viscoelastic pipe flow

Ming Dong^{1,†} and Mengqi Zhang^{2,†}

¹State Key Laboratory of Nonlinear Mechanics, Institute of Mechanics, Chinese Academy of Sciences, Beijing 100190, PR China

²Department of Mechanical Engineering, National University of Singapore, 9 Engineering Drive 1, 117575 Singapore

(Received 19 April 2021; revised 13 December 2021; accepted 29 December 2021)

It is recently found that viscoelastic pipe flows can be linearly unstable, leading to the possibility of a supercritical transition route, in contrast to Newtonian pipe flows. Such an instability is referred to as the centre mode, which was studied numerically by Chaudhary *et al.* (*J. Fluid Mech.*, vol. 908, 2021, p. A11) based on an Oldroyd-B model. In this paper, we are interested in expanding the parameter space investigated and exploring the asymptotic scalings related to this centre instability in the Oldroyd-B viscoelastic pipe flow. It is found from the asymptotic analysis that the centre mode exhibits a three-layered asymptotic structure in the radial direction, a wall layer, a main layer and a central layer, which are driven by pure viscosity, axial and/or radial pressure gradient, and a combined effect of viscosity and elasticity, respectively. Depending on the relations of the control parameters, two regimes, the long-wavelength and short-wavelength centre instabilities, emerge, for which the central-layer thicknesses are of different orders of magnitude. Our large-Reynolds-number asymptotic predictions are compared to the numerical solutions of the original eigenvalue system, and favourable agreement is achieved, especially when the parameters approach their individual limits. In addition to revealing the dominant factors and their balances, the asymptotic analysis describes the instability system by reducing the number of control parameters, and furthermore explaining the collapse of the numerical results for different re-scalings.

Key words: viscoelasticity, polymers, shear-flow instability

1. Introduction

Fluid dynamics in a viscoelastic flow has been studied for a long time, but still fascinates researchers today owing to its great potential application in skin drag reduction and its

† Email addresses for correspondence: dongming@imech.ac.cn, mpezmq@nus.edu.sg

intriguing flow phenomena under different conditions (White & Mungal 2008; Graham 2014). The viscoelastic polymer solutions can exhibit Newtonian turbulence (where polymers stabilise the flow, leading to drag reduction), elastoinertial turbulence (EIT, where inertia and elasticity are comparable; see Samanta *et al.* 2013) and elastic turbulence (where the polymers destabilise the flow, resulting in a chaotic state; see Shaqfeh 1996; Groisman & Steinberg 2000) in a large parameter space. EIT can be considered as an intermediate state between Newtonian turbulence and elastic turbulence, and is the theme of study of this work.

Experimental evidence for EIT flow has been gathered in recent years. Its unique flow features and connection to the maximum drag reduction (MDR) state (which is a flow state where the drag reduction by polymers is maximum regardless of the polymers used; see Virk 1975) have been characterised. Samanta *et al.* (2013) first studied EIT experimentally. The flow phenomena in EIT are fundamentally different from those in Newtonian turbulence. In EIT, the most salient features are the tilted shear layers close to the walls elongated in the streamwise direction, and a high spatial correlation of the flow structures in the spanwise direction, clearly demonstrated in their three-dimensional (3-D) numerical simulations (see also later work, (Lopez, Choueiri & Hof 2019), on viscoelastic pipe flows). In Newtonian turbulence, localised flow structures prevail and spatiotemporal intermittency is strong. Strictly two-dimensional (2-D) EIT simulations have also been produced successfully in channels (Sid, Terrapon & Dubief 2018; Shekar *et al.* 2019; Zhu & Xi 2021). Additionally, Samanta *et al.* (2013) found that the friction factor of EIT can be continued smoothly to the asymptotic MDR results when Re (the Reynolds number) is increased, suggesting that EIT may be dynamically relevant to the flows in the MDR regime. Later, in their experimental investigations of EIT, Choueiri, Lopez & Hof (2018) observed that in a range of polymer concentrations, the MDR limit can in fact be exceeded in the results of the friction factor. More specifically, with increasing polymer concentration, the turbulent flow can be fully relaminarised (where the drag reduction is greater than the MDR) before becoming unstable and arriving in the MDR limit. The flow structures in MDR are similar to those of EIT, reinforcing the perspective that there is a strong connection between the EIT and MDR regimes. In a viscoelastic channel flow, Page, Dubief & Kerswell (2020) first showed that the arrowhead structures in EIT flows strongly suggest a connection to the bifurcation of the centre-mode linear instability (Ram & Tamir 1964; Garg *et al.* 2018) – to be discussed below – although these structures may not be a necessary condition for the transitional EIT (Samanta *et al.* 2013; Sid *et al.* 2018); bifurcating from a wall mode has been demonstrated in Shekar *et al.* (2019). Subsequent experimental evidence for the resemblance between the EIT flow structures at the onset and the centre mode was presented by Choueiri *et al.* (2021) in a viscoelastic pipe flow, although the experimental flow exhibits a weakly chaotic and distorted nature.

Furthermore, the authors have explored smaller values of Re (prior to onset) and found that EIT can also emerge in these subcritical conditions, showing similar chevron-shaped structures, which obviates a supercritical route. Garg *et al.* (2018) and Chaudhary *et al.* (2021) interpreted the bifurcation curve (with respect to Re) in the results of Samanta *et al.* (2013) as an indication of a supercritical bifurcation, but Choueiri *et al.* (2021) stated that the heuristic loop may be difficult to observe in such experiments because the amplitude threshold to trigger the subcritical transition may be so low that the inherent disturbance in the experimental facilities is enough to render the flow unstable. Similar numerical evidence was provided by Shekar *et al.* (2019) in their high-Weissenberg-number (Wi) simulation. Finally, flows far from the instability onset (in the large- Re range) can also

exhibit a pattern of tilted streamwise streaks, which have been observed in previous experimental and numerical works on EIT (Dubief, Terrapon & Soria 2013; Samanta *et al.* 2013; Sid *et al.* 2018; Shekar *et al.* 2019, 2021). Again, in this regime (large Re), the continuous transition from the EIT to the MDR limit has been established, but the underlying mechanism of MDR is EIT associated to the wall mode. In particular, for another parameter set, the work of Shekar *et al.* (2021) demonstrated how the sheetlike structures emerge directly from the Newtonian nonlinear Tollmien–Schlichting (TS) waves.

Along with the experimental explorations, direct numerical simulations (DNS) have been conducted to study EIT and MDR. Xi & Graham (2010*a,b*), utilising a minimal channel to simulate the turbulent viscoelastic flows, described MDR flows as a marginal Newtonian turbulent state. They found intervals of hibernating turbulence in which many flow characteristics of MDR can be observed. Later, more works started to recognise the important role of elasticity and focused on EIT in their DNS studies, accompanying the experimental works as reviewed above. Dubief *et al.* (2013) found similar turbulence statistics and flow structures in 2-D and 3-D EIT flows, demonstrating that a 2-D instability mechanism may be relevant in the 3-D turbulent flows. They also investigated the effect of artificial diffusion on the generation of EIT, and found that artificial diffusion can significantly affect EIT flow because the latter is essentially driven by small flow scales. (The necessity to use artificial diffusion is because of the hyperbolic nature of the polymer conformation equations (Kupferman 2005), and this technique has become popular since the pioneering work of Sureshkumar & Beris (1995).) Terrapon, Dubief & Soria (2014) took the divergence of the momentum equation to yield a balance of the Laplacian of the pressure with its inertial and elastic contributions. The elastic contribution, even though smaller, cannot be neglected especially when Wi , characterising the ratio between polymer relaxation time and flow turnover time, is relatively large. Their results also supported the smooth transition of EIT flow to MDR when Re increases. Lopez *et al.* (2019) simulated viscoelastic pipe flows near the transitional Re . They found that when Wi and the polymer maximum extension (in the FENE-P model, finitely extensible nonlinear elastic with the Peterlin closer) are sufficiently large, EIT flows correspond to the MDR limit, both of which can be considered to be disconnected from the Newtonian-type turbulence. More recently, Zhu & Xi (2021), in their numerical simulations of EIT flows, found that even though the drag reduction percentages of EIT flows can be similar in the MDR regime, the detailed flow dynamics (for example, the instantaneous friction factor as discussed by the authors) may differ from each other, indicating the complex nature of these flows despite the asymptotic drag-reduction results (which has also been shown and discussed earlier in Choueiri *et al.* 2018). They reported flows in the MDR regimes that are dissimilar to 2-D EIT.

In addition to DNS, theoretical analyses have also been applied to understand viscoelastic flows. Based on a resolvent analysis and DNS, Shekar *et al.* (2019) demonstrated that the resolvent mode with the greatest energy amplification (exploiting the non-normal nature of the underlying linear operator) appears to be very similar to the phase-averaged DNS results in the parameter range of EIT (at relatively large Re), both showing an elongated tilted pattern in the polymer fluctuation field. The most important eigenmode in this perspective is the TS wall mode, coupled with the critical-layer mechanism. Most of the studies mentioned above investigated EIT in subcritical routes; Graham (2014) has envisioned a supercritical route from the laminar polymeric flow to the MDR when the elastic effect is sufficiently strong. A linearly unstable centre mode

in viscoelastic pipe flows was later found by Garg *et al.* (2018) and was characterised further in Chaudhary *et al.* (2021). The unstable mode is propagating at a phase speed close to the centreline velocity of the base flow. The scalings in the results of neutral curves were identified, to be discussed in § 2.3. Comparisons to experiments (Samanta *et al.* 2013; Chandra, Shankar & Das 2018) were discussed, including that the invariant results in Samanta *et al.* (2013) to external disturbance lent support to a supercritical route (but note the explanation by Choueiri *et al.* (2021) on the disturbance threshold of subcritical transition). The critical Re_c by the linear theory is also close to that in Chandra *et al.* (2018), but the scaling of Re_c with respect to $E(1 - \beta)$ in the linear theory needs modifications, probably due to the ignorance of the shear-thinning effect in the Oldroyd-B model, where E is the elastic number ($E = Re/Wi$), and β is the ratio of the solvent viscosity to the total viscosity. The supercritical bifurcation route originating from the linear instability in the EIT parameter range was advertised by these authors as a new pathway to MDR, supplementing the elastically modified Newtonian route (for which it is notable that strong amplification of the disturbance energy exists in viscoelastic channel and pipe flows Shekar *et al.* 2019; Zhang 2021). The more realistic FENE-P model has been implemented in the linear stability analysis of viscoelastic pipe flows in Zhang (2021) to tackle the effect of finite maximal extension of polymers (the Oldroyd-B model allows for infinitely long polymers), and it is found that a smaller maximal extensibility has a stabilising effect on the flow. More recently, starting numerically from this centre-mode instability, Page *et al.* (2020) and Dubief *et al.* (2021) computed the exact coherent structures in 2-D viscoelastic channel flows of FENE-P fluids in subcritical conditions by using the Newton–Krylov method and arc-length continuation. The solutions take the shape of an arrowhead structure and travel at a phase speed that is close to the centre mode.

Traditionally, the wall mode in Newtonian shear flows has been studied extensively by asymptotic techniques. As summarised by Drazin & Reid (2004), the instability modes in an incompressible channel flow can be described by two types of asymptotic structures: the lower-branch and upper-branch instabilities. Both belong to the wall mode, which is driven by pure viscosity and so is also referred to as the viscous TS mode. In the large- Re limit, the lower-branch wall mode exhibits a double-layered structure: an inviscid main (outer) layer and a viscous wall (inner) layer. The thickness of the latter is of $O((k Re)^{1/3} h)$, where h is the half-width of the channel. Incompressible boundary layer flows also support the lower-branch (Lin 1946; Smith 1979) and upper-branch (Smith 1981) TS instabilities. In the large- Re framework, the lower-branch TS mode is described by the triple-deck formalism, in which the viscous lower deck interacts with the inviscid upper deck, forming a pressure–displacement interaction.

However, the wall mode in Newtonian pipe flows never becomes linearly unstable, rendering a subcritical route of Newtonian pipe flow transition. Only when the polymer effect is present can the pipe flow become unstable, and as mentioned above, the instability nature is changed to the centre-mode instability. However, the centre-mode instability, although it has been studied numerically in a certain parameter space, is still lacking insightful observations from the asymptotic point of view. For example, in Chaudhary *et al.* (2021), it is observed that the neutral curves and eigenfunctions for different parameters could collapse under certain regularisation, and the neutral curves for a low-concentration configuration show a double-lobe structure, indicating a double-unstable-mode nature. However, we do not know the salient asymptotic structures leading to the collapse or the reason for the emergence of the additional unstable mode. In fact, the viscoelastic central-mode instability is more complicated due to its dependence on a greater number of

control parameters than the Newtonian flow instability, and solving numerically the linear eigenvalue system as in Garg *et al.* (2018) and Chaudhary *et al.* (2021) is not sufficient to reveal its intrinsic mechanism and to draw generic conclusions. Therefore, in this work, we will carry out an asymptotic analysis of the centre-mode instability in Oldroyd-B pipe flows.

The paper is organised as follows. In § 2, we describe the physical problem to be studied and introduce its governing equations. In §§ 3 and 4, respectively, we conduct asymptotic analysis of the long- and short-wavelength centre modes. Note that the long-wavelength instability regime is also valid when the wavelength is comparable with the pipe radius, as will be proven in Appendix B. In § 5, the asymptotic equations in §§ 3 and 4 are solved numerically, which is confirmed by comparing with the numerical solutions of the original linear system and those in the literature. Finally, § 6 concludes the paper with some discussions.

2. Mathematical descriptions

2.1. Physical problem and the governing equations

The physical model to be studied is a polymer-solution flow in a round pipe. The flow field is analysed in the cylindrical coordinate system (z, r, θ) , with z, r and θ denoting the axial, radial and azimuthal directions, respectively. The pipe radius R is selected as the reference length, and the velocity field $\mathbf{u} = (u_z, u_r, u_\theta)$, time t and pressure p are normalised by $U_{max}, R/U_{max}$ and ρU_{max}^2 , respectively, where ρ is the density of the fluid, and U_{max} is the maximum (centreline) velocity of the laminar pipe flow. The conformation tensor \mathbf{c} and stress $\boldsymbol{\tau}_p$ are normalised by $k_B T/H$ and $\mu_p U_{max}/R$, respectively, where k_B is the Boltzmann constant, T is temperature, H is the spring constant in the elastic dumbbell model of the polymer, and μ_p is the additional fluid viscosity due to the polymer (Bird *et al.* 1987). The flow motions are characterised by, among others, two dimensionless parameters, a Reynolds number and a Weissenberg number, which are defined as

$$Re = \frac{\rho U_{max} R}{\mu}, \quad Wi = \frac{\lambda U_{max}}{R}, \tag{2.1a,b}$$

where μ and λ are the total viscosity and the relaxation time of the polymer molecules (to their equilibrium states), respectively. In particular, the total viscosity is the sum of the solvent viscosity μ_s and the polymer viscosity μ_p , i.e. $\mu = \mu_s + \mu_p$, and a viscosity ratio β is defined as

$$\beta = \frac{\mu_s}{\mu} \in [0, 1]. \tag{2.2}$$

Note that if $\beta = 1$, then the flow is Newtonian, while $\beta = 0$ corresponds to the upper-convective-Maxwell (UCM) flow. The Oldroyd-B model is assumed (Bird *et al.* 1987), and the dimensionless Navier–Stokes equations and the constitutive equations are

$$\nabla \cdot \mathbf{u} = 0, \quad \frac{\partial \mathbf{u}}{\partial t} + \mathbf{u} \cdot \nabla \mathbf{u} = -\nabla p + \frac{\beta}{Re} \nabla^2 \mathbf{u} + \frac{1-\beta}{Re} \nabla \cdot \boldsymbol{\tau}_p, \tag{2.3a,b}$$

$$\boldsymbol{\tau}_p = \frac{\mathbf{c} - \mathbf{I}}{Wi}, \quad \frac{\partial \mathbf{c}}{\partial t} + \mathbf{u} \cdot \nabla \mathbf{c} - \mathbf{c} \cdot (\nabla \mathbf{u}) - (\nabla \mathbf{u})^T \cdot \mathbf{c} = -\boldsymbol{\tau}_p, \tag{2.3c,d}$$

where \mathbf{I} denotes the unity matrix. Note that the Oldroyd-B model is an idealised model that assumes the polymer extensibility to be infinitely strong, which is sufficient to demonstrate the instability mechanism and convenient for analysis; therefore, we do not consider

here the more realistic FENE-P model (where the effect of finite extensibility can be studied); see Zhang *et al.* (2013), Lopez *et al.* (2019), Page *et al.* (2020) and Zhang (2021). As a systematic investigation, in the following we will visit the centre-mode instability in a complete set of the parameter space, which may include some unattainable Wi in experiments.

The flow field $\phi = (\mathbf{u}, p, c_{11}, c_{12}, c_{22}, c_{13}, c_{23}, c_{33})$ is decomposed into a steady mean flow $\Phi = (U, P, C_{11}, C_{12}, C_{22}, C_{13}, C_{23}, C_{33})$ and a harmonic perturbation

$$\phi = \Phi(r) + \hat{\epsilon} \hat{\phi}(r) e^{i(kz+2\pi m\theta - \omega t)} + \text{c.c.}, \tag{2.4}$$

where $\hat{\phi} = (\hat{\mathbf{u}}, \hat{p}, \hat{c}_{11}, \hat{c}_{12}, \hat{c}_{22}, \hat{c}_{13}, \hat{c}_{23}, \hat{c}_{33})$, $\hat{\epsilon} \ll 1$ denotes the amplitude, k is the axial wavenumber, m is the number of waves in the azimuthal direction, ω is the frequency, and c.c. denotes the complex conjugate. In a temporal stability analysis, k is taken to be real, and $\omega = \omega_r + i\omega_i$ is complex, with the imaginary part representing the temporal growth rate. In this paper, we restrict our attention to the axisymmetric mode, for which $m = 0$.

The base states $\Phi(r)$ for the velocity and conformation tensor field are expressed as

$$U = (U, 0, 0) \text{ with } U = 1 - r^2, \quad C = \begin{pmatrix} 1 + 2Wi^2 U'^2 & Wi U' & 0 \\ Wi U' & 1 & 0 \\ 0 & 0 & 1 \end{pmatrix}, \tag{2.5a,b}$$

where throughout this paper a prime denotes the derivative with respect to its argument.

In the above formulation, the conformation tensor is analysed in the sense of Reynolds decomposition, which has been adopted by many recent works on the centre-mode instability, such as Garg *et al.* (2018), Page *et al.* (2020) and Chaudhary *et al.* (2021). We note that Hameduddin *et al.* (2018) and Hameduddin, Gayme & Zaki (2019) have recently proposed a new decomposition method based on a geometric understanding of the differential deformation of the polymers, being able to guarantee the positive-definiteness of the conformation tensor. For stability analyses of non-turbulent viscoelastic flows, the results of the two decomposition methods can be consistent with each other; see the comparisons in Zhang (2021), Wan, Sun & Zhang (2021) and Buza, Page & Kerswell (2021).

2.2. Instability mode

After substituting (2.3c,d) into the governing equations (2.3) and retaining the $O(\hat{\epsilon})$ terms, we arrive at a linear system of $\hat{\phi}$ for $m = 0$:

$$ik\hat{u}_z + \hat{u}'_r + \hat{u}_r/r = 0, \tag{2.6a}$$

$$ik(U - c)\hat{u}_z + U'\hat{u}_r + ik\hat{p} = \frac{\beta}{Re}(\hat{u}''_z + \hat{u}'_z/r - k^2\hat{u}_z) + \frac{1 - \beta}{Re Wi}(ik\hat{c}_{11} + \hat{c}'_{12} + \hat{c}_{12}/r), \tag{2.6b}$$

$$ik(U - c)\hat{u}_r + \hat{p}' = \frac{\beta}{Re}(\hat{u}''_r + \hat{u}'_r/r - k^2\hat{u}_r - \hat{u}_r/r^2) + \frac{1 - \beta}{Re Wi}(ik\hat{c}_{12} + \hat{c}'_{22} + \hat{c}_{22}/r - \hat{c}_{33}/r), \tag{2.6c}$$

$$(ik(U - c) + Wi^{-1})\hat{c}_{11} + C'_{11}\hat{u}_r - 2(ikC_{11}u_z + C_{12}\hat{u}'_z + U'\hat{c}_{12}) = 0, \tag{2.6d}$$

$$(ik(U - c) + Wi^{-1})\hat{c}_{12} + C'_{12}\hat{u}_r - (ikC_{12}u_z + C_{22}\hat{u}'_z + U'\hat{c}_{22} + ikC_{11}\hat{u}_r + C_{12}\hat{u}'_r) = 0, \tag{2.6e}$$

Asymptotic study of instability in a viscoelastic pipe

$$(ik(U - c) + Wi^{-1})\hat{c}_{22} - 2(ikC_{12}u_r + C_{22}\hat{u}'_r) = 0, \tag{2.6f}$$

$$(ik(U - c) + Wi^{-1})\hat{c}_{33} - 2C_{33}\hat{u}_r/r = 0, \tag{2.6g}$$

where $c \equiv \omega/k = c_r + ic_i$, with c_r denoting the phase speed. This system is an extension of the Orr–Sommerfeld equations, and so is referred to as the EOS system in this paper. No-slip, non-penetration conditions are imposed at the wall:

$$\hat{u}_z(1) = \hat{u}_r(1) = 0. \tag{2.7a,b}$$

At the centreline, the radial velocity must vanish due to the symmetric nature, and we obtain from the continuity equation that the axial velocity must have zero gradient. Therefore, the boundary conditions at $r = 0$ are

$$\hat{u}'_z(0) = \hat{u}_r(0) = 0. \tag{2.8a,b}$$

2.3. Brief overview of numerical solutions of the EOS system

Using numerical code as implemented in Zhang (2021), we can obtain solutions to the EOS system (2.6) with boundary conditions (2.7) and (2.8). The calculated eigenspectra, including the continuous and discrete modes, are compared with those of Chaudhary *et al.* (2021) in Appendix A, and favourable agreement is achieved.

The linear system (2.6) is dependent on four control parameters, Re , Wi , k and β , and the unstable centre mode appears in a certain range of them. For a fixed β , the critical parameters Re_c , Wi_c and k_c , depicting the onset of axisymmetric neutral instability, form a three-dimensional curve in the Re – Wi – k space. For demonstration, we choose $\beta = 0.9$ and plot the projections of this curve onto the Re – Wi and k – Wi planes in figures 1(a) and 1(b), respectively. The unstable zone appears when Wi is greater than approximately 56, and two critical neutral curve branches appear for each supercritical Wi . As Wi becomes large, k_c for the lower-branch neutral curve is decreasing, whereas k_c for the upper-branch neutral curve is increasing. A similar plot can be found in Buza *et al.* (2021) for an FENE-P channel flow.

By visiting a large set of control parameters, Chaudhary *et al.* (2021) presented interesting observations on the centre instability. (1) For fixed β and $E \equiv Re/Wi$, the neutral curves in the Re – k and c_r – k planes exhibit scattered behaviour without any regular pattern; however, when they are plotted in $Re E^{3/2}$ – $kE^{1/2}$ and $(1 - c_r)/E$ – $kE^{1/2}$ planes, the curves with different E collapse perfectly. (2) In the limit as $\beta \rightarrow 1$, the neutral curves can be scaled in the $Re[(1 - \beta)E]^{3/2}$ – $k[(1 - \beta)E]^{1/2}$ plane. (3) By use of regular perturbation techniques, two regimes, with central-layer thicknesses $O(Re^{-1/3}R)$ and $O(Re^{-1/4}R)$, respectively, were found, which are able to predict the numerical eigenfunctions for a few selections of parameters. However, these observations lack in-depth explanations, and the physical origin of the centre-mode instability remains unclear. As the lower and upper branches of the neutral curve shown in figure 1 correspond to low and high limits of the critical wavenumbers, respectively, it is natural to link these two limits to the potentially distinguished long- and short-wavelength regimes in the asymptotic framework, respectively. Analysis of these regimes could explain the numerical observations of Chaudhary *et al.* (2021), and shed light on the key mechanism of the centre-mode instability, which is to be presented in §§ 3 and 4.

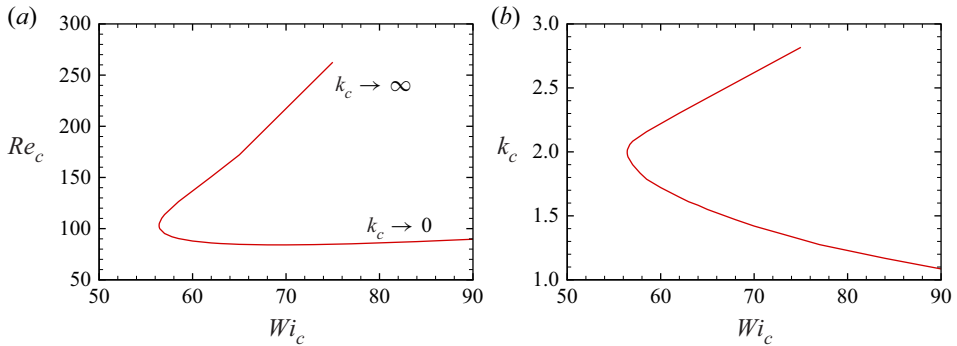


Figure 1. Projections of the critical neutral curve for $\beta = 0.9$ and $m = 0$ in the $Wi-Re$ (a) and $Wi-k$ (b) planes.

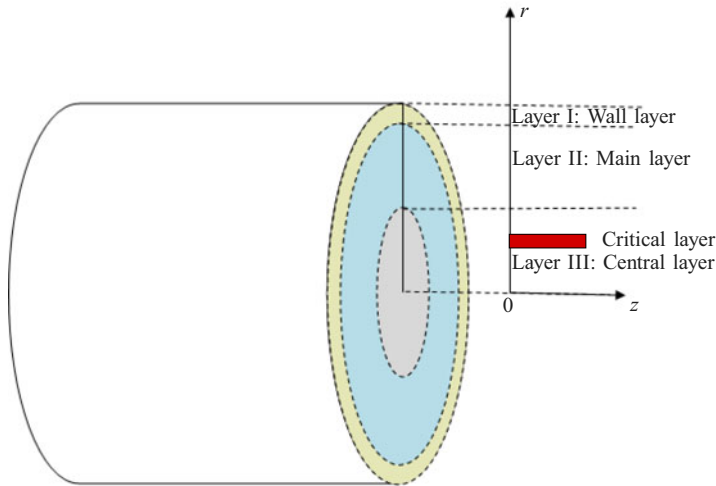


Figure 2. A sketch of the multi-layered structure for long-wavelength centre modes in a viscoelastic pipe flow. The critical layer appears only for near-neutral low-concentration centre modes.

2.4. Summary of the overall structures of the asymptotic regimes

Before illustrating the mathematical details of the asymptotic regimes, we summarise the salient observations from §§ 3 and 4. A schematic of the multi-layered structure for both the long- and short-wavelength regimes is shown in figure 2. Usually, three asymptotic layers, including a wall layer, a main layer and a central layer, appear in the radial direction, but an additional critical layer may appear when the concentration is low ($\beta \rightarrow 1$) and the mode is near neutral. Table 1 summarises the asymptotic scalings and the thickness of each asymptotic layer, where a few quantities are to be defined in the following two sections. Readers can use this table as a guide to understand §§ 3 and 4.

Note that in the regular-concentration regime, as will be discussed in §§ 3.1 and 4.1, no singularity appears in the central-layer solution, so the critical layer is not needed. However, we do need a critical layer in the low-concentration regime, as will be shown in §§ 3.2 and 4.2.

	§ 3: long-wavelength regime $Re^{-1} \ll k \leq O(1)$		§ 4: short-wavelength regime $k \gg 1$	
	§ 3.1 regular concentration ($\beta, 1 - \beta$) = $O(1)$	§ 3.2 low concentration $1 - \beta \ll 1$	§ 4.1 regular concentration ($\beta, 1 - \beta$) = $O(1)$	§ 4.2 low concentration $1 - \beta \ll 1$
Scaling	$Wi \sim k^{-1/2} Re^{1/2}$	$Wi \sim \frac{k^{-1/2} Re^{1/2}}{1 - \beta}$	$Re \sim k^3, Wi \sim k$	$Re \sim k^3, Wi \sim \frac{k}{1 - \beta}$
Similarity parameters	W_1, β	\bar{W}	R_3, W_3, β	R_3, \bar{W}_3
$1 - c$		$O(k^{-1/2} Re^{-1/2})$		$O(k^{-2})$
Wall layer		$1 - r = O(k^{-1/2} Re^{-1/2})$		$1 - r = O(k^{-2})$
Main layer		$r = O(1)$		$r = O(1)$
Central layer		$r = O(k^{-1/4} Re^{-1/4})$		$r = O(k^{-1})$
Critical layer	—	$O\left(\frac{1 - \beta}{k^{1/4} Re^{1/4}}\right)$	—	$O\left(\frac{1 - \beta}{k}\right)$

Table 1. Summary of the asymptotic regimes, including the scaling relations of the control parameters, similarity parameters and thickness of each asymptotic layer in viscoelastic pipe flows.

3. Long-wavelength centre mode

In the asymptotic framework, the Reynolds number is taken to be sufficiently large,

$$Re \gg 1, \tag{3.1}$$

and the centre mode is referred to as an instability mode whose eigenfunction is concentrated near the centreline, thus its phase speed is close to, but less than unity:

$$0 < 1 - c_r \ll 1. \tag{3.2}$$

In the long-wavelength regime, we assume the wavenumber to be small, but still greater than Re^{-1} , i.e.

$$Re^{-1} \ll k \ll 1, \tag{3.3}$$

such that the radial momentum equation is reduced to $\hat{p}' \approx 0$, and \hat{c}_{33} never appears in the leading-order hydrodynamic motions. It is noted that this instability regime is also applicable when the wavenumber satisfies $k = O(1)$, as is proven in [Appendix B](#). For convenience, this mode is referred to as the long-wavelength centre mode.

In the following two subsections, §§ 3.1 and 3.2, we will present singular perturbation analysis to uncover the asymptotic structures of the long-wavelength centre mode for regular-level concentration ($(\beta, 1 - \beta) = O(1)$) and low-level concentration ($0 < 1 - \beta \ll 1$), respectively. A discussion on the instability mechanism will be presented in § 3.3.

3.1. Asymptotic analysis for a regular-level concentration

The viscosity ratio in this subsection is assumed to be $O(1)$, but not close to unity:

$$\beta = O(1), \quad 1 - \beta = O(1). \tag{3.4a,b}$$

Preliminary asymptotic analysis indicates that three asymptotic layers appear in the radial direction, as listed in [table 1](#). In the wall layer, the viscosity appears at leading order, and from balance of the convective and viscous terms, we obtain the thickness of the wall layer,

$$1 - r = O(k^{-1/2} Re^{-1/2}). \tag{3.5}$$

The central layer may be driven by either viscosity or elasticity. From balance of the convective term of the conformation tensor $ik(U - c)\hat{c}_{ij}$ with the conformation stress $Wi^{-1}\hat{c}_{ij}$, noticing that $U = 1 - r^2$ and the phase speed c is rather close to 1, we can estimate the thickness of the elastic central layer as

$$r = O(k^{-1/2} Wi^{-1/2}). \tag{3.6}$$

On the other hand, from balance of the convective terms in the axial momentum equation with the viscous terms, we obtain the thickness of the viscous central layer as

$$r = O(k^{-1/4} Re^{-1/4}). \tag{3.7}$$

Note that the thicknesses of the two central layers are usually of different magnitudes, depending on the values of the control parameters, Re , Wi and k . In this paper, we will show that an unstable centre mode could appear when the thicknesses of the two layers are comparable, which leads to a scaling law

$$Wi \sim k^{-1/2} Re^{1/2}, \tag{3.8}$$

rendering a viscoelasticity instability nature.

For convenience, we introduce

$$R_1 = Re/\beta, \quad W_1 = k^{1/2}R_1^{-1/2}Wi, \quad W_2 = \beta W_1/(1 - \beta). \quad (3.9a-c)$$

From assumptions (3.1) and (3.4a,b), we know that $R_1 = O(Re)$ and $(W_1, W_2) = O(1)$. In the central layer, from (3.6) or (3.7), balance of the axial momentum equation determines that the correction of the phase speed is $O(r^2) = O(k^{-1/2}R_1^{-1/2})$. Therefore, we expand the complex phase speed in terms of an asymptotic series

$$c = 1 + k^{-1/2}R_1^{-1/2}c_1 + \dots, \quad (3.10)$$

in which the first term on the right-hand side, 1, comes from the centreline velocity of the base flow. The next task is to solve for c_1 to gain a more quantitative understanding of the instability. In the following three subsections, we will show the leading-order governing equations and their solutions for the three asymptotic layers.

3.1.1. Main-layer solutions

In the main layer (layer II of figure 2), we obtain from the continuity equation (2.6a) that $\hat{u}_r \sim k\hat{u}_z$. Balance of the conformation equations determines $\hat{c}_{11} \sim k^{-1}R_1\hat{u}_z$, $\hat{c}_{12} \sim R_1\hat{u}_z$ and $\hat{c}_{22} \sim k^{1/2}R_1^{1/2}\hat{u}_z$. Therefore, the perturbation field is expanded as

$$(\hat{u}_z, \hat{u}_r, \hat{p}) = (\hat{u}_0, k\hat{v}_0, \hat{p}_0) + k^{-1/2}R_1^{-1/2}(\hat{u}_1, k\hat{v}_1, \hat{p}_1) + \dots, \quad (3.11a)$$

$$(\hat{c}_{11}, \hat{c}_{12}, \hat{c}_{22}) = (k^{-1}R_1\hat{c}_{11,0}, R_1\hat{c}_{12,0}, k^{1/2}R_1^{1/2}\hat{c}_{22,0}) + \dots. \quad (3.11b)$$

In the main layer, the viscosity and polymer stress tensor play minor roles to the momentum convection, so the leading-order governing equations for the hydrodynamic perturbations are

$$i\hat{u}_0 + \hat{v}'_0 + \hat{v}_0/r = 0, \quad -ir^2\hat{u}_0 - 2r\hat{v}_0 + i\hat{p}_0 = 0, \quad \hat{p}'_0 = 0, \quad (3.12a-c)$$

which implies the inviscid nature to leading-order accuracy. The solutions of (3.12) are $\hat{u}_0 = 2iA_1$, $\hat{v}_0 = i\hat{p}_0/(2r) + A_1r$, with A_1 being an arbitrary constant. These solutions do not satisfy the no-slip condition at the wall, $r = 1$, which indicates that a viscous wall layer (layer I) must be taken into account. The analysis of this layer is the same as that of the Stokes layer in Goldstein (1985), Liu, Dong & Wu (2020) and Dong, Liu & Wu (2020). It was shown that the radial velocity \hat{v}_r is much smaller than the axial velocity \hat{v}_z due to its thin-layer property, which determines the boundary condition of the main layer at the wall, $\hat{v}_0(1) = 0$. A direct consequence is $A_1 = -i\hat{p}_0/2$. Therefore, the solutions of the leading-order velocities are

$$\hat{u}_0 = \hat{p}_0, \quad \hat{v}_0 = \frac{i\hat{p}_0}{2} \left(\frac{1}{r} - r \right). \quad (3.13a,b)$$

The governing equations for the leading-order conformation tensor are

$$-ir^2\hat{c}_{11,0} + 16W_1^2r\hat{v}_0 + 4r\hat{c}_{12,0} - 16W_1^2ir^2\hat{u}_0 = 0, \quad (3.14a)$$

$$-ir^2\hat{c}_{12,0} - 8ir^2W_1^2\hat{v}_0 = 0, \quad -ir^2\hat{c}_{22,0} + 4irW_1\hat{v}_0 = 0, \quad (3.14b,c)$$

whose solutions are

$$\hat{c}_{11,0} = -16iW_1^2\hat{v}'_0, \quad \hat{c}_{12,0} = -8W_1^2\hat{v}_0, \quad \hat{c}_{22,0} = \frac{4W_1}{r}\hat{v}_0. \quad (3.15a-c)$$

The second-order hydrodynamic perturbations are governed by

$$i\hat{u}_1 + \hat{v}'_1 + \hat{v}_1/r = 0, \tag{3.16a}$$

$$-i r^2 \hat{u}_1 - 2r \hat{v}_1 + i \hat{p}_1 = i c_1 \hat{u}_0 + W_2^{-1} (i \hat{c}_{11,0} + \hat{c}'_{12,0} + \hat{c}_{12,0}/r), \quad \hat{p}'_1 = 0, \tag{3.16b,c}$$

from which we obtain

$$\hat{v}_1 = \frac{i \hat{p}_1}{2r} + i \hat{p}_0 \left(\frac{2W_1^2 W_2^{-1}}{r^3} - \frac{c_1}{2r} \right) - \left(\frac{i \hat{p}_1}{2} + i \hat{p}_0 (2W_1^2 W_2^{-1} - c_1/2) + A_2 \right) r, \tag{3.17}$$

where A_2 is a constant. In principle, A_2 can be determined by matching with the wall-layer solution, but it is not needed in the following analysis.

Combining (3.13a,b) and (3.16a), we obtain the asymptotic behaviours of the velocity field in the limit as $r \rightarrow 0$:

$$\hat{u}_r \rightarrow \frac{i \hat{p}_0}{2} k \left(\frac{1}{r} + \dots + 4k^{-1/2} R_1^{-1/2} W_1^2 W_2^{-1} \frac{1}{r^3} + \dots \right), \tag{3.18a}$$

$$\hat{u}_z \rightarrow \hat{p}_0 \left(1 + \dots + 4k^{-1/2} R_1^{-1/2} W_1^2 W_2^{-1} \frac{1}{r^4} + \dots \right). \tag{3.18b}$$

Obviously, these solutions cease to be valid when the high-order terms come to the leading order, which appears in the vicinity of the centreline. From (3.18b) we find that a sublayer appears when $r = O(k^{-1/8} R_1^{-1/8})$. However, a further analysis indicates that this layer is not a distinguished one because the leading-order impact does not change. From (3.18a) we find that a sublayer appears when $r = O(k^{-1/4} R_1^{-1/4})$, which is the same as the central layer (3.7).

3.1.2. Viscous wall layer

Since the inviscid solution in the main layer does not satisfy the no-slip condition at the wall, a wall (Stokes) layer for which $1 - r = O(k^{-1/2} R_1^{-1/2})$ needs to be considered. For convenience, we introduce a local coordinate

$$\hat{y} = (1 - r)k^{1/2} R_1^{1/2} = O(1). \tag{3.19}$$

The flow field is expanded as

$$(\hat{u}_z, \hat{u}_r, \hat{p}) = \hat{p}_0 (\hat{u}_w, k^{1/2} R_1^{-1/2} \hat{v}_w, \hat{p}_w) + \dots, \tag{3.20}$$

and the influence of the polymer stress is of high-order impact in this layer.

The leading-order governing equations in the wall layer are

$$i\hat{u}_w + \hat{v}'_w = 0, \quad -i\hat{u}_w - i\hat{p}_w - \hat{u}''_w = 0, \quad \hat{p}'_w = 0. \tag{3.21a-c}$$

Eliminating \hat{v}_w and \hat{p}_w , we obtain

$$\hat{u}_w = \hat{p}_w \left(1 - \exp(e^{3\pi i/4} \hat{y}) \right). \tag{3.22}$$

Matching with the main-layer solution, we obtain that $\hat{p}_w = 1$.

3.1.3. Central layer

Because the expansion (3.11a) breaks down in the $O(k^{-1/4}R_1^{-1/4})$ vicinity of the centreline, we need to carry out an analysis in this layer. For convenience, we introduce the local coordinate

$$\tilde{y} = k^{1/4}R_1^{1/4}r = O(1). \tag{3.23}$$

The perturbation field is now expanded as

$$(\hat{v}_z, \hat{v}_r, \hat{p}) = \hat{p}_0(k^{1/2}R_1^{1/2}\tilde{u}, k^{5/4}R_1^{1/4}\tilde{v}, 1) + \dots, \tag{3.24a}$$

$$(\hat{c}_{11}, \hat{c}_{12}, \hat{c}_{22}) = \hat{p}_0(k^{-1/2}R_1^{3/2}\tilde{c}_{11}, k^{1/4}R_1^{5/4}\tilde{c}_{12}, kR_1\tilde{c}_{22}) + \dots. \tag{3.24b}$$

Substitution of (3.24) into (2.6) leads to

$$i\tilde{u} + \tilde{v}' + \tilde{v}/\tilde{y} = 0, \tag{3.25a}$$

$$-i(\tilde{y}^2 + c_1)\tilde{u} - 2\tilde{y}\tilde{v} + i = \tilde{u}'' + \tilde{u}'/\tilde{y} + W_2^{-1}(i\tilde{c}_{11} + \tilde{c}'_{12} + \tilde{c}_{12}/\tilde{y}), \tag{3.25b}$$

$$\tilde{L}\tilde{c}_{11} = 16iW_1^2\tilde{y}^2\tilde{u} - 4W_1\tilde{y}\tilde{u}' - 4\tilde{y}\tilde{c}_{12} - 16W_1^2\tilde{y}\tilde{v}, \tag{3.25c}$$

$$\tilde{L}\tilde{c}_{12} = \tilde{u}' - 2iW_1\tilde{y}\tilde{u} - 2\tilde{y}\tilde{c}_{22} - 2W_1\tilde{y}\tilde{v}' + 2W_1\tilde{v} + 8i\tilde{y}^2W_1^2\tilde{v}, \tag{3.25d}$$

$$\tilde{L}\tilde{c}_{22} = 2\tilde{v}' - 4iW_1\tilde{y}\tilde{v}, \tag{3.25e}$$

where $\tilde{L} \equiv -i(\tilde{y}^2 + c_1) + W_1^{-1}$. In (3.25b), both the viscosity and the polymer stress tensor appear at leading order, therefore this equation is not singular at any radial position. In (3.25c-e), it is seen that there is no viscous-like term (second-order derivative with respect to \tilde{y}) on the right-hand sides, and a singularity is possible when $\tilde{L} = 0$, which, however, occurs only for $c_{1,i} = -W_1^{-1}$. Since $W_1 > 0$, such a condition implies that the eigenmode is stable with an exponentially decaying manner, which is of little interest in our study. Therefore, in the following analysis of the long-wavelength regular-concentration unstable (or marginally unstable) mode, we do not need a critical layer.

Note that the equation system does not admit closed-form analytical solutions, so we seek help from numerics. In the numerical process, the system (3.25) can be recast to a group of first-order differential equations

$$\frac{d\tilde{\phi}}{d\tilde{y}} = \tilde{L}\tilde{\phi}, \tag{3.26}$$

where $\tilde{\phi} = (\tilde{u}, \tilde{u}', \tilde{u}'', \tilde{v})^T$ and the non-zero elements of \tilde{L} are

$$\tilde{L}_{12} = 1, \quad \tilde{L}_{23} = 1, \quad \tilde{L}_{31} = \frac{16W_1^2\tilde{y}(\tilde{y}^4 - c_1^2)}{\tilde{L}^2(1 + W_2\tilde{L})}, \quad \tilde{L}_{41} = -i, \quad \tilde{L}_{44} = -1/\tilde{y}, \tag{3.27}$$

$$\tilde{L}_{32} = \frac{8\tilde{y}^4 - 8\tilde{y}^2(i + 2W_1\tilde{y}^2)\tilde{L} + (1 + 8iW_1\tilde{y}^2 + 8W_1^2\tilde{y}^4)\tilde{L}^2}{\tilde{y}^2\tilde{L}^2(1 + W_2\tilde{L})} + \frac{W_2(1 - i\tilde{y}^2(\tilde{y}^2 + c_1))\tilde{L}^3}{\tilde{y}^2\tilde{L}^2(1 + W_2\tilde{L})}, \tag{3.28}$$

$$\tilde{L}_{33} = -\frac{4i\tilde{y}^2 + \tilde{L} - 4i\tilde{W}_1\tilde{y}^2\tilde{L} + W_2\tilde{L}^2}{\tilde{y}\tilde{L}(1 + W_2\tilde{L})}, \quad \tilde{L}_{34} = -\frac{32iW_1^2\tilde{y}^2(\tilde{y}^2 - c_1)}{\tilde{L}^2(1 + W_2\tilde{L})}. \tag{3.29}$$

Matching with the main-layer solutions (3.18b), we obtain the matching conditions

$$\tilde{u} \rightarrow \frac{4W_1^2W_2^{-1}}{\tilde{y}^4} + o(\tilde{y}^{-4}), \quad \tilde{v} \rightarrow \frac{i}{2\tilde{y}} + O(\tilde{y}^{-3}) \quad \text{as } \tilde{y} \rightarrow \infty. \tag{3.30a,b}$$

In the numerical process, this condition can be recast as

$$(\tilde{u}', \tilde{u}'') \rightarrow 0 \quad \text{at } \tilde{y} = \tilde{y}_n, \tag{3.31}$$

with $\tilde{y}_n \gg 1$ being the upper boundary of the computational domain. The boundary conditions at the centreline are

$$\tilde{u}'(0) = \tilde{v}(0) = 0. \tag{3.32}$$

The system (3.26) with (3.31) and (3.32) is to be solved numerically by the same approach as in Dong & Wu (2013) and Wu & Dong (2016). It is obvious from this system that for a given β , the eigenvalue, c_1 , and the eigenfunctions depend on only one parameter, $W_1 = k^{1/2}R_1^{-1/2}Wi$, which reduces the complexity of the original eigenvalue system remarkably. Practically, with the assumptions (3.1) and (3.9a–c), we know that Wi has to be much greater than unity. For a given β that is not close to unity, the unstable centre modes would appear in a certain range of W_1 , and the unstable region of Wi increases with $Re^{1/2}$ and decreases with $k^{-1/2}$.

3.2. Asymptotic analysis for a low-level concentration

As β approaches unity, W_2 in (3.9a–c) becomes much greater than 1, and the asymptotic analysis in § 3.1 needs to be modified. For convenience, we introduce

$$\sigma = \frac{1 - \beta}{\beta} \ll 1. \tag{3.33}$$

Balancing the leading-order terms in the central layer, we can work out that $W_1 \sim \sigma^{-1}$. Here we have assumed $k^{1/2}R_1^{-1/2} \ll \sigma \ll 1$. For convenience, we introduce an $O(1)$ parameter \bar{W} such that

$$W_1 = \sigma^{-1}\bar{W}, \quad W_2 = \sigma^{-2}\bar{W}. \tag{3.34a,b}$$

The complex phase speed is now expanded as

$$c = 1 + k^{-1/2}R_1^{-1/2}(\bar{c}_1 + \sigma\bar{c}_2) + \dots \tag{3.35}$$

In the following, we will study the three asymptotic layers in the low-concentration configuration. The overall process is the same as that in § 3.1, but in this regime, a critical layer, as sketched in figure 2, appears in the central layer when the mode is neutral.

3.2.1. Main layer

Following the same procedure as in § 3.1.1, we obtain the main-layer radial velocity perturbation in the limit as $r \rightarrow 0$:

$$\hat{u}_r \rightarrow \frac{i\hat{P}_0}{2}k \left(\frac{1}{r} + \dots + 4k^{-1/2}R_1^{-1/2}\bar{W}\frac{1}{r^3} + \dots \right), \tag{3.36}$$

where \hat{P}_0 denotes the pressure perturbation in the main layer. Note that the solutions in the wall layer (3.20) stay unchanged.

3.2.2. Central layer

The thickness of the central layer in this regime is the same as that in § 3.1.3, so \tilde{y} in (3.23) is still the local coordinate. The perturbation field is expanded as

$$(\hat{v}_z, \hat{v}_r, \hat{p}) = \hat{p}_0[k^{1/2}R_1^{1/2}(\tilde{U}_0 + \sigma\tilde{U}_1), k^{5/4}R_1^{1/4}(\tilde{V}_0 + \sigma\tilde{V}_1), (1 + \sigma\tilde{P}_1)] + \dots, \quad (3.37a)$$

$$(\hat{c}_{11}, \hat{c}_{12}, \hat{c}_{22}) = \hat{p}_0(k^{-1/2}R_1^{3/2}\sigma^{-2}\tilde{C}_{11}, k^{1/4}R_1^{5/4}\sigma^{-2}\tilde{C}_{12}, kR_1\sigma^{-1}\tilde{C}_{22}) + \dots. \quad (3.37b)$$

Since W_1 and W_2 are much greater than 1, the leading-order governing equations are changed to

$$i\tilde{U}_0 + \tilde{V}'_0 + \tilde{V}_0/\tilde{y} = 0, \quad (3.38a)$$

$$\tilde{L}_1\tilde{U}_0 - 2\tilde{y}\tilde{V}_0 + i = \tilde{U}''_0 + \tilde{U}'_0/\tilde{y} + \bar{W}^{-1}(i\tilde{C}_{11,0} + \tilde{C}'_{12,0} + \tilde{C}_{12,0}/\tilde{y}), \quad (3.38b)$$

$$\tilde{L}_1\tilde{C}_{11,0} = 16i\bar{W}^2\tilde{y}^2\tilde{U}_0 - 4\tilde{y}\tilde{C}_{12,0} - 16\bar{W}^2\tilde{y}\tilde{V}_0, \quad (3.38c)$$

$$\tilde{L}_1\tilde{C}_{12,0} = 8i\tilde{y}^2\bar{W}^2\tilde{V}_0, \quad \tilde{L}_1\tilde{C}_{22,0} = -4i\bar{W}\tilde{y}\tilde{V}_0, \quad (3.38d,e)$$

where $\tilde{L}_1 = -i(\tilde{y}^2 + \bar{c}_1)$. Comparing with (3.25), it is found that a few terms in the conformation tensor equations move to the high order. However, they may become the leading-order impact if $\tilde{L}_1 \approx 0$ somewhere inside the central layer. This situation occurs when the mode to leading order is neutral, i.e. \bar{c}_1 is real and negative. Therefore, for the neutral case, a critical layer around $\tilde{y}_c = \sqrt{-\bar{c}_1}$, with thickness $\tilde{y} - \tilde{y}_c = O(\sigma)$ (or $r - r_c = O(\sigma k^{-1/4}R_1^{-1/4})$ with $r_c = k^{-1/4}R_1^{-1/4}\tilde{y}_c$), must be taken into account; see the red region of figure 2. A detailed analysis of the critical layer is provided in Appendix C.

Being similar to (3.26), the system (3.38) is recast to

$$\frac{d\tilde{\phi}_0}{d\tilde{y}} = L\tilde{\phi}_0, \quad (3.39)$$

where $\tilde{\phi}_0 = (\tilde{U}_0, \tilde{U}'_0, \tilde{U}''_0, \tilde{V}_0)^T$ and

$$L = \begin{pmatrix} 0 & 1 & 0 & 0 \\ 0 & 0 & 1 & 0 \\ \frac{16\bar{W}\tilde{y}(2i\tilde{y}^2 + \tilde{L}_1)}{\tilde{L}_1^2} & \frac{1}{\tilde{y}^2} + \frac{8\bar{W}\tilde{y}^2}{\tilde{L}_1} + \tilde{L}_1 & -\frac{1}{\tilde{y}} & \frac{-32\bar{W}\tilde{y}^2(2i\tilde{y}^2 + \tilde{L}_1)}{\tilde{L}_1^3} \\ -i & 0 & 0 & -1/\tilde{y} \end{pmatrix}. \quad (3.40)$$

The linear system (3.39) is subject to the matching and boundary conditions (3.31) and (3.32), with (\hat{u}, \hat{v}) being replaced by (\hat{U}_0, \hat{V}_0) .

In order to obtain \bar{c}_2 , we need to consider the second-order perturbations, which are governed by

$$\left(\frac{d}{d\tilde{y}} - L\right)\tilde{\phi}_1 = b, \quad (3.41)$$

where $\tilde{\phi}_1 = (\tilde{U}_1, \tilde{U}'_1, \tilde{U}''_1, \tilde{V}_1)^T$ and $\mathbf{b} = (0, 0, b_1\bar{c}_2 + b_2, 0)$, with

$$b_1 = \frac{8\bar{W}\tilde{y}}{\tilde{L}_1^4}[-8\tilde{y}\tilde{L}_1(\tilde{y}\tilde{U}_0 + i\tilde{V}_0) + 24\tilde{y}^3\tilde{V}_0 + i\tilde{L}_1^2(2\tilde{U}_0 + \tilde{y}\tilde{U}'_0)] - i\tilde{U}'_0, \quad (3.42)$$

$$b_2 = \frac{4i}{\tilde{L}_1^4}[-24\tilde{y}^2\tilde{L}_1(\tilde{y}\tilde{U}_0 + i\tilde{V}_0) + 48\tilde{y}^4\tilde{V}_0 + 6i\tilde{y}\tilde{L}_1^2(2\tilde{U}_0 + \tilde{y}\tilde{U}'_0) + \tilde{L}_1^3(2\tilde{U}'_0 + \tilde{y}\tilde{U}''_0)]. \quad (3.43)$$

The adjoint vector $\psi^\dagger = (\psi_1^\dagger, \psi_2^\dagger, \psi_3^\dagger, \psi_4^\dagger)^T$ of the differential equation (3.39) satisfies

$$\left(\frac{d}{d\tilde{y}} + L^T\right)\psi^\dagger = 0, \quad (3.44)$$

with the matching and boundary conditions

$$\psi_{2,3}^\dagger(\tilde{y}) \rightarrow 0 \text{ as } \tilde{y} \rightarrow \infty, \quad \psi_1^\dagger(0) = \psi_3^\dagger(0) = 0. \quad (3.45a,b)$$

After multiplying both sides of (3.41) by $(\psi^\dagger)^T$ and integrating from $\tilde{y} = 0$ to ∞ , we obtain the second-order correction of the phase speed:

$$\bar{c}_2 = -\frac{\int_0^\infty \psi_3^\dagger b_2 d\tilde{y}}{\int_0^\infty \psi_3^\dagger b_1 d\tilde{y}}. \quad (3.46)$$

3.3. Discussion of the instability mechanism

From the analysis of the three-layered structure of the long-wavelength central mode, we can summarise the instability mechanism in this subsection. The most distinguished layer is the central layer, since the perturbation damps algebraically approaching the main layer. Also, the viscous wall layer is passive and the perturbations there are at most comparable with those in the main layer.

In the central layer, where $r \ll 1$, the polymer stress in the momentum equation is usually less significant than the viscous term, because the viscous term has a second-order derivative with respect to r but the polymer stress has only a first-order derivative. However, the magnitude of the polymer stress increases drastically with Wi , which can be explained as follows. In this thin layer, the mean conformation tensors \mathbf{C}_{11} and \mathbf{C}_{12} are large for $Wi \gg 1$, while the mean velocity U is not affected by Wi , with the magnitudes of U' and $1 - U$ becoming small as r reduces. Thus it is seen from balance of the conformation tensor equations that the conformation perturbations are much greater than the velocity perturbations, which leads to a possible balance of the viscous and polymer stress terms in the momentum equation. This is true when a careful choice of Wi , namely, $Wi \sim k^{-1/2}Re^{1/2}$ for regular concentration and $Wi \sim \sigma^{-1}k^{-1/2}Re^{1/2}$ for low concentration, is implemented. Under these parameter scalings, all the terms – the inertia, pressure gradient, viscosity and polymer stress – are retained in the leading-order momentum equations in the central layer, implying a rather complicated process. Such an instability mechanism is also true for the short-wavelength regimes, as will be shown in the next section.

As will be shown in § 5, there would be an additional unstable branch when β is sufficiently close to unity, in which the unstable region of the parameter W_1 would be extended to infinity. The high- W_1 limit of the long-wavelength centre mode is analysed in Appendix D. It is found that for $W_1 \gg 1$, the dominant factors in the central layer are redistributed in three sublayers. The bulk central layer where $\tilde{y} = O(1)$ is dominated only by balance of the inertia and pressure gradient; the outer central layer where $\tilde{y} = O(W_1^{1/2})$ is dominated by balance of the inertia and polymer stress; the core central layer where $\tilde{y} = O(W_1^{-1/2})$ is dominated by balance of the viscosity and polymer stress. These results regarding the dominant factors in the centre-mode instability have not been discussed in the literature.

4. Short-wavelength centre mode

In § 4.2 of Chaudhary *et al.* (2021), it was found that the neutral curves may be extended to the region where the axial wavenumber k is high, which leads to another type of instability, the short-wavelength centre mode. We will perform an asymptotic analysis for this regime in the regular-concentration and low-concentration configurations in §§ 4.1 and 4.2, respectively. For brevity, the duplicated illustrations are removed.

4.1. Asymptotic analysis for a regular-level concentration

In this regime, the leading-order balance of the central layer is the same as that in the long-wavelength regime, so the relation (3.8) is also valid. However, because in this regime $k \gg 1$, we obtain from balance of the leading-order terms of the linearised system (2.6) in each layer that the instability appears when

$$Re = O(k^3), \quad Wi = O(k), \quad \beta = O(1), \tag{4.1a-c}$$

therefore a group of $O(1)$ parameters is introduced:

$$R_3 = k^{-3}Re/\beta, \quad W_3 = k^{-1}R_3^{-1/2}Wi, \quad W_4 = \beta W_3/(1 - \beta). \tag{4.2a-c}$$

By scaling analysis as in the previous section, we expand the complex phase speed as

$$c = 1 + k^{-2}R_3^{-1/2}\hat{c}_1 + \dots \tag{4.3}$$

The asymptotic structure of the instability is the same as in figure 2, which is to be analysed in the following subsections.

4.1.1. Main-layer solution

Being similar to the long-wavelength mode, the governing equations in the main layer are inviscid to leading-order accuracy. The short-wavelength perturbation usually oscillates rapidly in the transverse direction, leading to a multiple-scale manner in the r -direction,

so the Wentzel–Kramers–Brillouin (WKB) form perturbations are assumed:

$$(\hat{u}_z, \hat{u}_r, \hat{p}) \sim (C_u^-, C_v^-, C_p^-) e^{-k\Theta_0(r)+\Theta_1(r)+\dots} + (C_u^+, C_v^+, C_p^+) e^{k\Theta_0(r)+\Theta_1(r)+\dots}, \quad (4.4)$$

where $C_u^\pm, C_v^\pm, C_p^\pm$ are coefficients, and Θ_0 and Θ_1 are functions of r . Upon substituting the solution form into the governing equations (2.6) and eliminating \hat{u}_z and \hat{p} , we obtain

$$\hat{u}_r'' + \frac{1}{r}\hat{u}_r' - k^2\hat{u}_r = O(1). \quad (4.5)$$

Substituting (4.4) into (4.5) and retaining the $O(k^2)$ and $O(k)$ terms, we obtain $\Theta_0'^2 = 1$ and $\Theta_0'' + 2\Theta_0'\Theta_1' + \Theta_1'/r = 0$, respectively. Without loss of generality, we choose

$$\Theta_0 = r, \quad \Theta_1 = -\frac{1}{2} \ln r. \quad (4.6a,b)$$

From the continuity and axial-momentum equations, we obtain

$$C_u^\pm = \pm i C_v^\pm, \quad C_p^\pm = \pm i r^2 C_v^\pm. \quad (4.7a,b)$$

Being similar to that in the long-wavelength regime, the non-penetration condition, $\hat{u}_r(1) = 0$, is introduced, which leads to

$$C_v^- = -e^{2k} C_v^+. \quad (4.8)$$

As $r \rightarrow 0$, both \hat{u}_z and \hat{u}_r grow like $r^{-1/2}$, and by use of the singular perturbation approach, we must consider a thin layer around the centreline. Obviously, the expansion (4.4) ceases to be valid when $k\Theta_0' \sim \Theta_1'$, which appears when $r \sim k^{-1}$, and this is indeed the thickness of the central layer.

4.1.2. Central-layer solution

In the central layer, we introduce a local coordinate

$$\tilde{Y} = kR_3^{1/4}r = O(1), \quad (4.9)$$

and the perturbation field is expanded as

$$(\hat{v}_z, \hat{v}_r, \hat{p}) = k^{1/2}(\check{U}, R_3^{-1/4}\check{V}, k^{-2}\check{P}) + \dots, \quad (4.10a)$$

$$(\hat{c}_{11}, \hat{c}_{12}, \hat{c}_{22}, \hat{c}_{33}) = k^{5/2}(R_3\check{C}_{11}, R_3^{3/4}\check{C}_{12}, R_3^{1/2}\check{C}_{22}, R_3^{1/2}\check{C}_{33}) + \dots. \quad (4.10b)$$

Note that in the above expansions, R_3 is of $O(1)$, which is introduced only for convenience of analysis.

By substituting (4.10a) into (2.6) and eliminating the conformation tensor perturbation, we obtain a fourth-order linear homogenous system

$$\frac{d\check{\Phi}}{d\check{Y}} = \bar{L}\check{\Phi}, \tag{4.11}$$

where $\check{\Phi} = (\check{U}, \check{U}', \check{U}'', \check{V})^T$, and the non-zero elements of \bar{L} are

$$\bar{L}_{12} = 1, \quad \bar{L}_{23} = 1, \quad \bar{L}_{41} = -i, \quad \bar{L}_{44} = -1/\check{Y}, \tag{4.12}$$

$$\bar{L}_{31} = \frac{16W_3^2\check{Y}(\check{Y}^4 - \hat{c}_1) - 4W_3\bar{L}\check{Y}(\check{Y}^2 + \hat{c}_1)R_3^{-1/2}}{\bar{L}^2(1 + W_4\bar{L})}, \tag{4.13}$$

$$\begin{aligned} \bar{L}_{32} = & \frac{8\check{Y}^4 - 8\check{Y}^2(i + 2W_3\check{Y}^2)\bar{L} + \bar{L}^2[1 + 8iW_3\check{Y}^2 + 8W_3^2\check{Y}^4]}{\check{Y}^2\bar{L}^2(1 + W_4\bar{L})} \\ & + \frac{W_4[1 - i\check{Y}^2(\hat{c}_1 + i\check{Y}^2)]\bar{L}^3}{\check{Y}^2\bar{L}^2(1 + W_4\bar{L})} + 2R_3^{-1/2}, \end{aligned} \tag{4.14}$$

$$\bar{L}_{33} = -\frac{4i\check{Y}^2 + \bar{L}(1 - 4iW_3\check{Y}^2) + W_4\bar{L}^2}{\check{Y}\bar{L}(1 + W_4\bar{L})}, \tag{4.15}$$

$$\bar{L}_{34} = -\frac{32iW_3^2\check{Y}^2(\check{Y}^2 - \hat{c}_1)}{\bar{L}^2(1 + W_4\bar{L})} - \frac{8i\check{Y}^2(1 + W_3^2\bar{L}^2) + W_4(\hat{c}_1 + \check{Y}^2)\bar{L}^3}{\bar{L}^2(1 + W_4\bar{L})}R_3^{-1/2} - iR_3^{-1}, \tag{4.16}$$

with $\bar{L} = -i(\check{Y}^2 + \hat{c}_1) + W_3^{-1}$. In this system, R_3 always appears with a negative power, $-1/2$ or -1 , implying that in the limit as $R_3 \rightarrow \infty$, the impact of R_3 becomes negligible. Again, the coefficient \check{L} could be zero only when $\hat{c}_{1,i} = -W_3^{-1}$, indicating a temporal decaying mode that is not of interest to us. The matching and boundary conditions are the same as (3.31) and (3.32). The eigenvalues and eigenfunctions of this system are to be solved by the same approaches as in § 3.1.3.

4.2. Asymptotic analysis for a low-level concentration

Now let us move on to the low-concentration regime. Being similar to the long-wavelength regime, we assumed that as $\sigma = (1 - \beta)/\beta \rightarrow 0$, the control parameters become

$$R_3 = O(1), \quad W_3 = O(\sigma^{-1}), \quad W_4 = O(\sigma^{-2}). \tag{4.17a-c}$$

Thus we introduce an $O(1)$ parameter \bar{W}_3 such that

$$W_3 = \sigma^{-1}\bar{W}_3, \quad W_4 = \sigma^{-2}\bar{W}_3, \tag{4.18a,b}$$

and the re-scaled complex phase-speed correction is expanded as

$$\hat{c}_1 = \hat{c}_{11} + \sigma\hat{c}_{12} + O(\sigma^2). \tag{4.19}$$

For brevity, in this subsection we skip the analysis in the main layer, and consider the leading-order governing equations only in the central layer, which can be expressed in

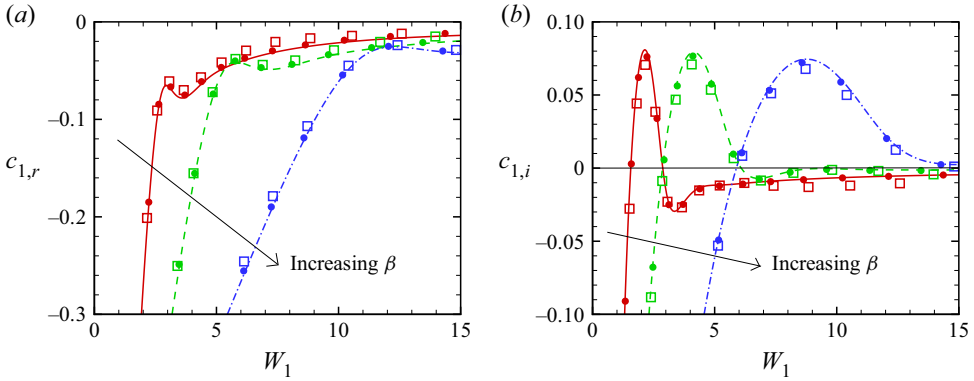


Figure 3. Dependence of the real (a) and imaginary (b) parts of c_1 on W_1 for $\beta = 0.65, 0.8$ and 0.9 . Continuous curves, asymptotic predictions from § 3.1; open squares, EOS solutions for $(k, Re) = (0.5, 2000)$; filled circles, EOS solutions for $(k, Re) = (0.5, 20000)$. The thin horizontal line in (b) represents $c_{1,i} = 0$.

terms of a linear homogeneous system

$$\frac{d\check{\Phi}_0}{d\check{Y}} = \hat{L}\check{\Phi}_0, \tag{4.20}$$

where $\check{\Phi}_0 = (\check{U}, \check{U}', \check{U}'', \check{V})$, and the non-zero elements of \hat{L} are

$$\hat{L}_{12} = 1, \quad \hat{L}_{23} = 1, \quad \hat{L}_{41} = -i, \quad \hat{L}_{44} = -1/\check{Y}, \tag{4.21}$$

$$\hat{L}_{31} = \frac{16\bar{W}_3\check{Y}(2i\check{Y}^2 + \hat{L})}{\hat{L}^2}, \quad \hat{L}_{32} = -i(\check{Y}^2 + \hat{c}_{11}) + \frac{1}{\check{Y}^2} + \frac{8\bar{W}_3\check{Y}^2}{\hat{L}} + 2R_3^{-1/2}, \tag{4.22}$$

$$\hat{L}_{33} = -\frac{1}{\check{Y}}, \quad \hat{L}_{34} = \frac{32i\bar{W}_3\check{Y}^2(\hat{c}_{11} - \check{Y}^2)}{\hat{L}^3} - \frac{8i\bar{W}_3\check{Y}^2 + (\hat{c}_{11} + \check{Y}^2)\hat{L}}{\hat{L}} R_3^{-1/2} - iR_3^{-1}, \tag{4.23}$$

with $\hat{L} = -i(\check{Y}^2 + \hat{c}_{11})$. This system is subject to the same boundary conditions as in § 4.1, and can be solved by the same numerical approach. Again, a critical layer appears in the region $\check{Y} - \sqrt{-\hat{c}_{11}} = O(\sigma)$ (or $r - k^{-1}\sqrt{-\hat{c}_{11}} = O(\sigma k^{-1})$) when the mode is neutral, namely, $\hat{c}_{11,i} = 0$. The solvability condition as for (3.46) is applied to solve \hat{c}_{12} .

5. Numerical results

After the theoretical development for the long- and short-wavelength instability modes, in this section we will solve numerically the asymptotic equations derived in previous sections and compare them to the numerical results of the EOS solutions and those in the literature.

5.1. Solutions for long-wavelength centre modes

For $\beta = O(1)$, $1 - \beta = O(1)$ and $k \leq O(1)$, the dispersion relation of the long-wavelength centre mode can be obtained by solving the eigenvalue system (3.25) with boundary conditions (3.31) and (3.32). The continuous curves in figures 3(a) and 3(b) respectively display this relation in the W_1 - $c_{1,r}$ and W_1 - $c_{1,i}$ planes for three representative β values.

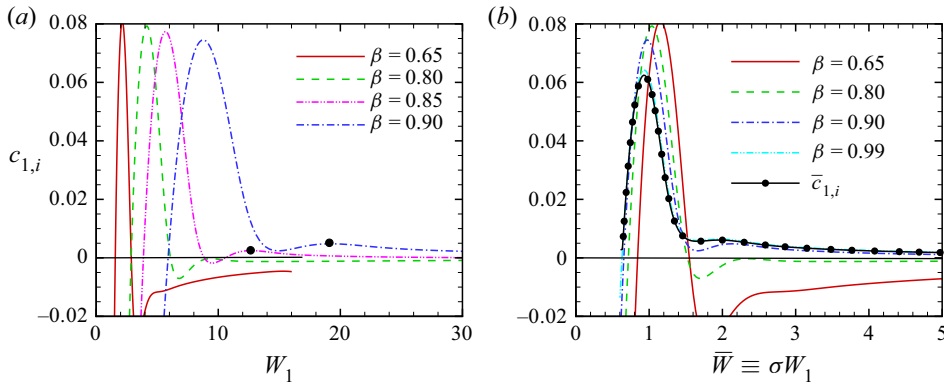


Figure 4. Dependence of $c_{1,i}$ on W_1 (a) and \bar{W} (b) for different β values, where the thin horizontal line represents $c_{1,i} = 0$, and the dots in (a) mark the second peaks of $c_{1,i}$. In (b), the black curve with circles denotes the low-concentration asymptotic prediction from § 3.2.

	$W_1^{(0)}$	$W_1^{(1)}$	$W_1^{(2)}$	$W_1^{(3)}$	$c_{1,r}^{(1)}$	$c_{1,r}^{(3)}$	$c_{1,i,max}$
$\beta = 0.65$	3.0	1.56	2.10	2.87	-0.460	-0.0650	0.0810
$\beta = 0.8$	5.80	2.86	4.14	6.09	-0.356	-0.0425	0.0790
$\beta = 0.9$	12.3	5.89	8.75	—	-0.270	—	0.077

Table 2. Key parameters characterising the instability property.

For each β , the real part $c_{1,r}$ increases with W_1 when the latter is small. After peaking at a certain value $W_1^{(0)}$, $c_{1,r}$ starts to decrease with W_1 mildly. A valley appears at a slightly higher W_1 , then $c_{1,r}$ increases with W_1 monotonically and approaches zero in the limit as $W_1 \rightarrow \infty$. The growth rate $c_{1,i}$ increases with W_1 from a negative value, and crosses the zero line at a certain W_1 , which is referred to as the lower-branch neutral point $W_1^{(1)}$. (Actually, the growth rate is defined as the imaginary part of the frequency $\omega_{1,i}$, but in this paper, we also call $c_{1,i}$ the growth rate for simplicity because they are related by $c_{1,i} = \omega_{1,i}/k$.) After peaking at $W_1^{(2)}$, the growth rate starts to decrease with W_1 . The greatest growth rate is denoted as $c_{1,i,max}$. For $\beta = 0.65$ and 0.8 , as W_1 further increases, $c_{1,i}$ crosses the zero line again at an upper-branch neutral point $W_1^{(3)}$, which is quite close to $W_1^{(0)}$. However, the curve for $\beta = 0.9$ does not have an upper-branch neutral point $W_1^{(3)}$, and its large- W_1 asymptotic behaviour is demonstrated in figure 4. The phase-speed corrections for the lower-branch ($W_1^{(1)}$) and upper-branch ($W_1^{(3)}$) neutral points are denoted as $c_{1,r}^{(1)}$ and $c_{1,r}^{(3)}$, respectively. The values of $W_1^{(0)}$, $W_1^{(1)}$, $W_1^{(2)}$, $W_1^{(3)}$, $c_{1,r}^{(1)}$ and $c_{1,r}^{(3)}$ are all increasing with β , and those for $c_{1,i,max}$ are decreasing, which is demonstrated in table 2. Choosing $k = 0.5$, and $Re = 2000$ and $20\,000$, we also obtain the dispersion relation by solving the EOS system (2.6) using the spectral collocation method as in Zhang (2021), and the results are shown by the open and filled symbols in figure 3, respectively. As expected, the EOS solutions agree with the asymptotic predictions quite well, and the agreement is better for a higher Reynolds number.

Figure 4(a) plots the $c_{1,i}$ - W_1 relations for a wider range of W_1 , with an additional curve for $\beta = 0.85$ added. Overall, the growth rate for each β shows two peaks, and the second peak is unstable only when β is sufficiently close to unity, i.e. $\beta > 0.8$. The implication is that when the concentration of the polymer is low, two unstable groups of centre modes appear, which are referred to as mode I and mode II. As $\beta \rightarrow 1$, the unstable region, including both modes, shifts towards the higher- W_1 direction. Such a phenomenon agrees with the analysis in § 3.2, namely, $W_1 \sim \sigma^{-1}$ as $\beta \rightarrow 1$ or $\sigma \rightarrow 0$ according to (3.34a,b). Therefore, we regularise the horizontal axis to $\bar{W} \equiv \sigma W_1$ and plot the growth rates in figure 4(b). In this panel, we also plot the low-concentration asymptotic prediction $\bar{c}_{1,i}$ from § 3.2. It is seen that as $\beta \rightarrow 1$, the solutions $c_{1,i}$ of the linear system (3.25) approach the asymptotic prediction $\bar{c}_{1,i}$ consistently.

The emergence of the second unstable region (mode II) for β close to unity has already been reported in figures 21 and 22 of Chaudhary *et al.* (2021); however, our result is still a bit surprising because mode II for a moderate W_1 is found to satisfy the same asymptotic scaling as that of mode I (they are solved by the same scaled governing equations, but mode II may show a new scaling in the large- W_1 limit). A clearer demonstration of mode II is shown in figure 5. Actually, the double-peak nature of the $c_{1,i}$ - W_1 curve, as shown in figure 4(a), determines the emergence of the two instability modes. Even for a lower β , e.g. $\beta = 0.65$, there are still overall two branches of modes separated by the local minimum value of $c_{1,i}$, but the second branch becomes unstable only when β is sufficiently close to unity. It is also seen that as $\beta \rightarrow 1$, W_1 of the upper neutral point of mode II approaches infinity, so mode II is linked directly to the large- W_1 behaviour of the long-wavelength instability. A salient nature of the unstable mode II for β sufficiently close to unity is that the growth rate is positive even when $W_1 \rightarrow \infty$, which leads to a high- W_1 (high- Wi) regime as analysed in Appendix D. It is shown that for a fixed β or σ , the growth rate $c_{1,i}$ decays like $W_1^{-1} c_{1,i}^\dagger$ as $W_1 \rightarrow \infty$ ($c_{1,i}^\dagger$ is defined in (D1)), whereas $c_{1,i}^\dagger$ scales as σ^{-1} as $\sigma \rightarrow 0$, leading to a scaling $c_{1,i} \sim (\sigma W_1)^{-1}$ in the limit as $\sigma W_1 \rightarrow \infty$. This is also inferred by the curves for $\beta = 0.99$ (light blue dot-dot-dashed line) and the low-concentration asymptote (black line with circles) in figure 4(b). It is also seen from figure 20 that when β is greater than 0.93, the upper-branch neutral W_1 moves to infinity. Therefore, in figure 4(b), the unstable region of mode II extends to $\bar{W} \rightarrow \infty$ for $\beta = 0.99$, but the curve for $\beta = 0.9$ will cross the zero line at somewhere out of the domain, $\bar{W} > 5$.

As shown by the pink line in figure 4(a), the growth rate $c_{1,i}$ for $\beta = 0.85$ crosses the zero line three times, and there is an additional neutral point above $W_1 = 30$. Mode I is located in the interval between the first two neutral points, while mode II appears when W_1 is above the third neutral point. For a smaller β , e.g. $\beta = 0.8$, mode II is stable, whereas for a greater β , e.g. $\beta = 0.9$, the upper-branch neutral point of mode I and the lower-branch neutral point of mode II merge, and the upper-branch neutral point of mode II starts to approach infinity. Figure 5 plots the \hat{u} - and \hat{v} -eigenfunctions of the four neutral points for $\beta = 0.85$. Their shapes are similar overall, but their local peaks and valleys move toward the high- \tilde{y} direction as W_1 increases.

A neutral curve delimits the marginally unstable relation for a certain set of control parameters, including Wi , Re , β and k . From the asymptotic analysis in § 3.1 we know that the control parameters can be reduced to W_1 and β , whose relation is shown by the red curves in figure 6(a). Here we show only the range of β from 0.3 to 1. Two unstable modes are clearly exhibited. The re-scaled Weissenberg number W_1 of the lower-branch neutral point of mode I increases with β like $0.6\sigma^{-1}$ (or $0.6\beta/(1-\beta)$), agreeing with the asymptotic prediction of § 3.2 (the lowest pink dashed line). For the upper-branch neutral point of mode I, W_1 increases with β up to a point $(\beta, W_1) = (0.87, 11.2)$, which

Asymptotic study of instability in a viscoelastic pipe

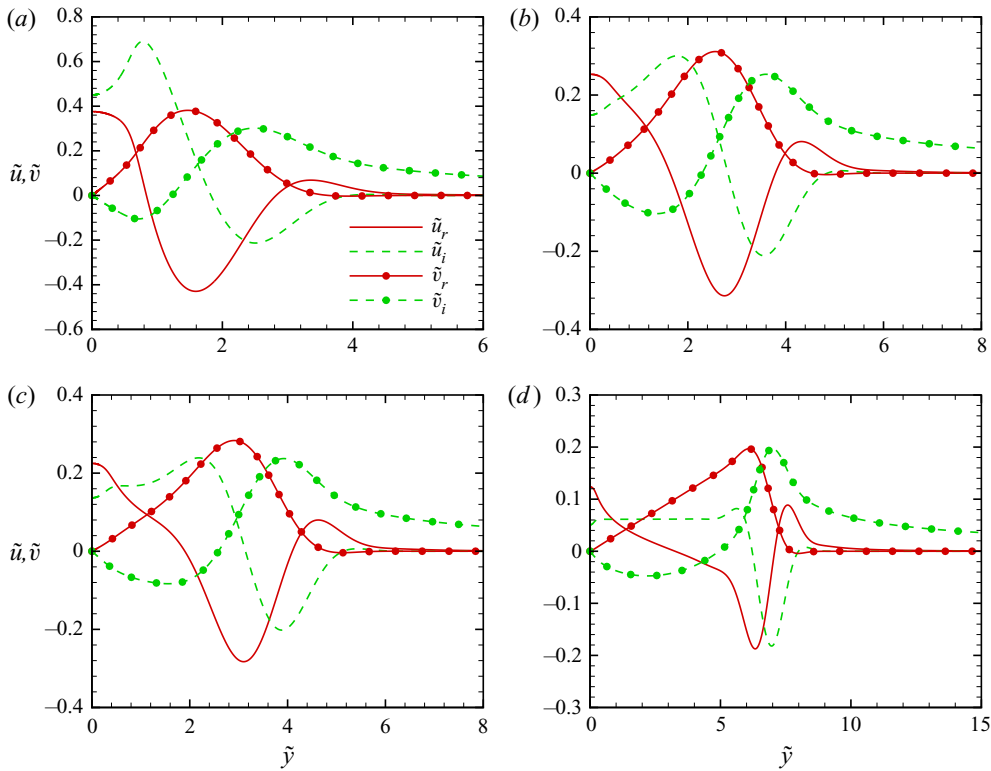


Figure 5. Transverse distribution of the eigenfunctions for $\beta = 0.85$. (a) Lower-branch neutral point of mode I, where $W_1 = 3.87$ and $c_1 = -0.316$; (b) upper-branch neutral point of mode I, where $W_1 = 8.85$ and $c_1 = -0.0373$; (c) lower-branch neutral point of mode II, where $W_1 = 10.57$ and $c_1 = -0.0392$; (d) upper-branch neutral point of mode II, where $W_1 = 34.3$ and $c_1 = -0.00848$.

connects the neutral curves of the two modes. Mode II first appears at $\beta \approx 0.805$, and its upper neutral curve approaches $W_1 = \infty$ as β increases. The solution for $\beta > 0.88$ is rather difficult to obtain, because as is illustrated in [Appendix D](#), the central layer splits into three asymptotic sublayers when $W_1 \gg 1$, which requires rather dense grid points near the core central region, and a sufficiently large computational domain to cover the outer central region. This information given by the asymptotic analysis may help in finite- Re calculations, which is another example of the value of asymptotic analysis. The phase-speed correction $-c_{1,r}$ of the two neutral modes is shown in [figure 6\(b\)](#); it decreases with β overall, and the decrease for the upper-branch neutral curve of mode II is extremely drastic.

The blue curves in [figures 6\(a–c\)](#) demonstrate the dispersion relation of the most unstable modes obtained by solving the eigenvalue system (3.25). It is obtained from the curves with circles in [figure 4\(b\)](#) that in the limit as $\beta \rightarrow 1$, the re-scaled Weissenberg numbers for the two peaks of the growth rates are $\bar{W} = \sigma W_1 = 0.92$ and 1.96 , respectively. The implication is that W_1 for the most unstable instabilities of the two modes in the low-concentration limit are $0.92\sigma^{-1}$ and $1.96\sigma^{-1}$, respectively, which are plotted by the pink dashed lines in [figure 6\(a\)](#). The agreement between the blue and pink curves as $\beta \rightarrow 1$ is quite good. Taking into account the leading- and second-order expansions in § 3.2, we find that as $\sigma \rightarrow 0$, the phase-speed corrections for the two modes decay like $0.069 + 0.58\sigma$ and $0.0123 + 0.163\sigma$, respectively. They are shown by

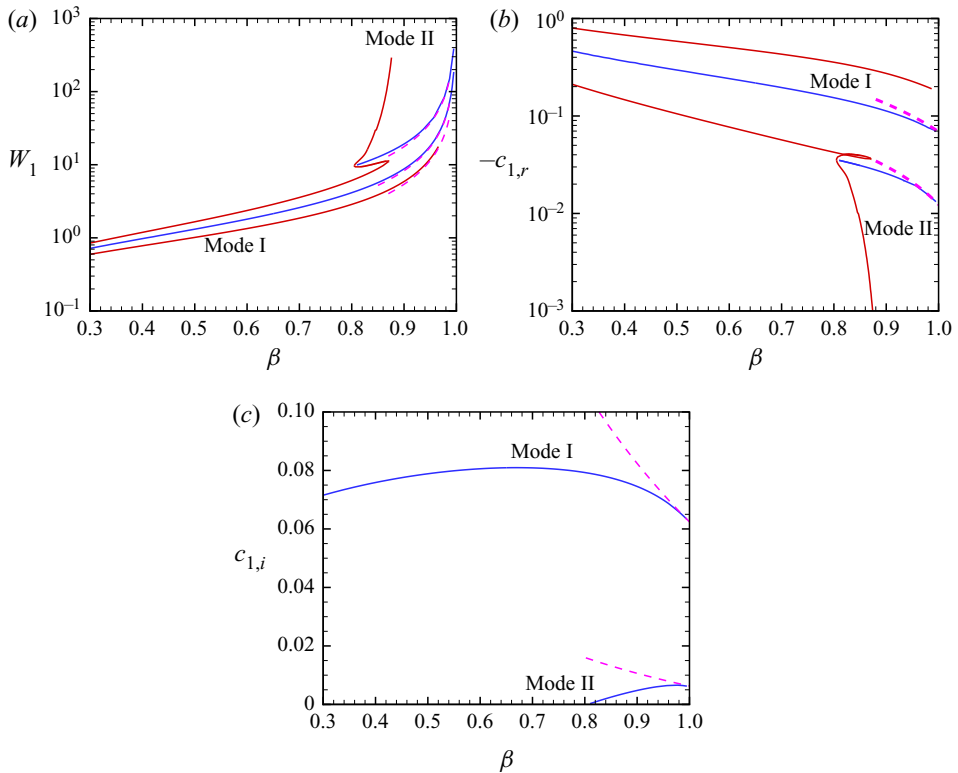


Figure 6. Dispersion relations of the neutral (red curves) and most unstable (blue curves) modes in the $W_1-\beta$ (a), $c_{1,r}-\beta$ (b) and $c_{1,i}-\beta$ (c) spaces. The pink dashed lines are the low-concentration asymptotic predictions.

the pink dashed curves in figure 6(b), agreeing with the blue curves when β approaches unity. In figure 6(c), the growth rate $c_{1,i}$ of mode I peaks at $\beta \approx 0.67$, and decays like $0.0624 + 0.18\sigma$ as $\beta \rightarrow 1$, agreeing with the low-concentration asymptotic prediction (pink dashed curves); the growth rate of mode II peaks at $\beta \approx 0.98$, and decays like $0.0063 + 0.039\sigma$ (low-concentration asymptotic prediction) as $\beta \rightarrow 1$.

Figures 7(a) and 7(b) compare the neutral curves obtained from the EOS solutions for different Re and k with the asymptotic predictions in figure 6. The agreement for mode I is quite satisfactory, but the EOS solutions for mode II scatter in a wide region. Overall, the EOS solutions approach the asymptotic prediction as Re increases, and for the same Re , the best agreement appears when $k = 0.5$ among the three k values considered here. It is noticed that the long-wavelength regime also works when $k = 1.0$, as is explained in Appendix B. Figure 7(c) displays the dependence of W_1 on β for the most unstable modes. The EOS solutions for the given parameters and the asymptotic predictions agree perfectly. Comparisons of the real and imaginary parts of c_1 of the most unstable modes are shown in figures 7(d) and 7(e). The greatest discrepancy appears for mode I, and again, the asymptotic predictions are more accurate to describe a higher- Re case.

5.2. Instability for short-wavelength modes

For $\beta = O(1)$, $1 - \beta = O(1)$ and $k \gg 1$, the short-wavelength mode is governed by the linear system (4.11), which is controlled by three independent parameters, β , R_3 and W_3 .

Asymptotic study of instability in a viscoelastic pipe

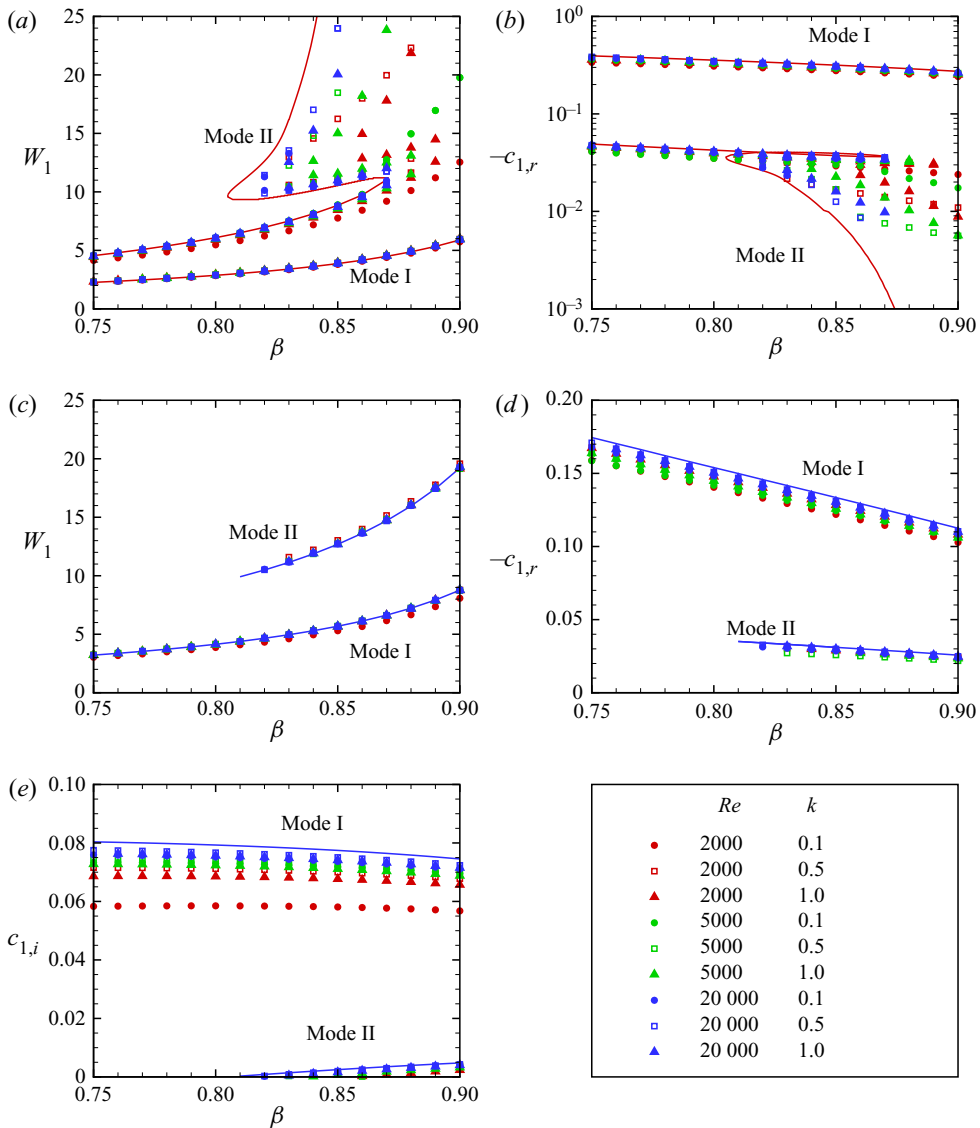


Figure 7. Comparison of the dispersion relations between the asymptotic predictions (continuous curves) and EOS solutions (symbols). (a, b) Neutral modes in the W_1 - β and $c_{1,r}$ - β spaces, respectively. (c, d, e) The most unstable modes in the W_1 - β , $c_{1,r}$ - β and $c_{1,i}$ - β spaces, respectively.

Note that W_4 is determined by W_3 and β . Figure 8 plots the dependence of \hat{c}_1 on W_3 for $R_3 = 25$ and three representative β values. Being similar to the long-wavelength regime, as shown in figure 3, the phase-speed correction $\hat{c}_{1,r}$ increases overall with W_3 , while $\hat{c}_{1,i}$ exhibits a local peak, with its maximum value increasing with β . When $\beta \geq 0.8$, an unstable region where $\hat{c}_{1,i} > 0$ is observed, which shifts to a higher W_3 as β increases.

As $\beta \rightarrow 1$, the instability approaches the low-concentration short-wavelength regime illustrated in § 4.2. Figure 9 changes the horizontal axis to $\bar{W}_3 = \sigma W_3$, and adds a case for $\beta = 0.99$. An asymptotic prediction given by the low-concentration short-wavelength regime, obtained by solving the linear system (4.20), is also plotted, where only the results

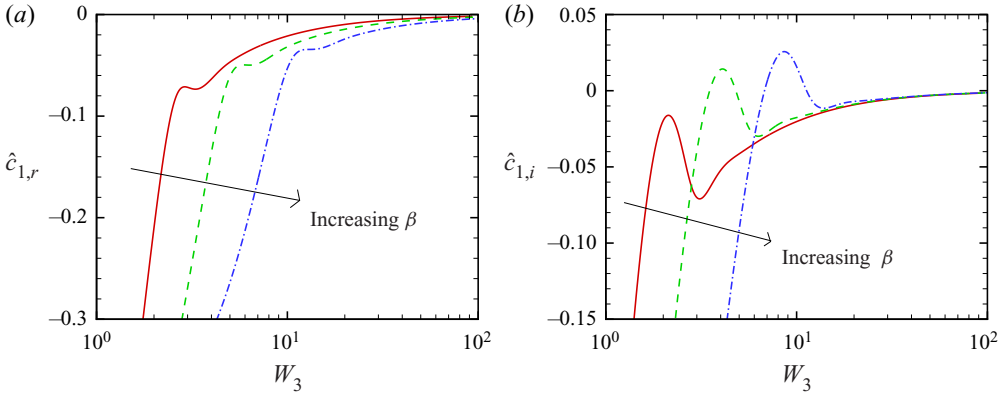


Figure 8. Dependence of the real (a) and imaginary (b) parts of \hat{c}_1 on W_3 for $\beta = 0.65, 0.8$ and 0.9 in the short-wavelength regime, where $R_3 = 25$.

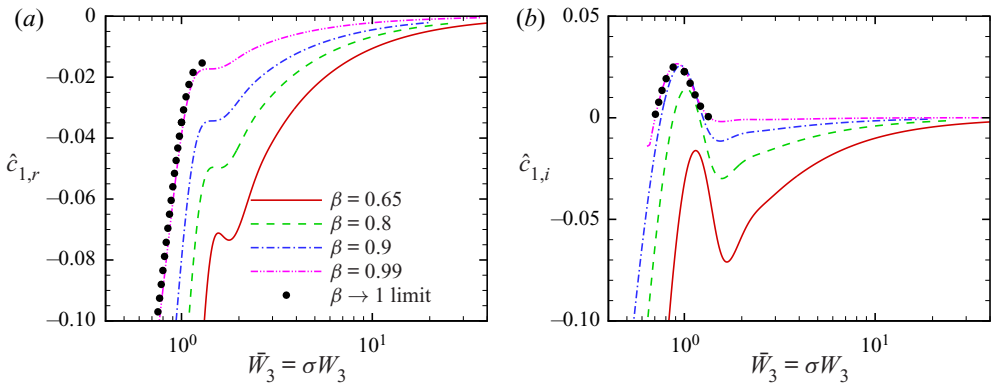


Figure 9. Dependence of the real (a) and imaginary (b) parts of \hat{c}_1 on \bar{W}_3 for $\beta = 0.65, 0.8, 0.9$ and 0.99 in the short-wavelength regime, where $R_3 = 25$.

in the unstable region are shown. Only one unstable mode is observed in this figure, but it should be noted that a mode II instability may also appear if R_3 is sufficiently large. It is seen that as $\beta \rightarrow 1$, the results predicted by (4.11) converge to those predicted by (4.20) consistently.

Figure 10 shows the dependence of the phase-speed correction on R_3 for a fixed \bar{W}_3 , but different β values. Both $\hat{c}_{1,r}$ and $\hat{c}_{1,i}$ approach constants as $R_3 \rightarrow \infty$, agreeing with the argument below (4.11). As $\beta \rightarrow 1$, \hat{c}_1 approaches the low-concentration asymptotic prediction illustrated in §4.2 (the black circles). In the large- R_3 limit, the latter also approaches a constant, $\hat{c}_1 = -0.0269 + 0.0518i$. It is seen from figure 10(b) that $\hat{c}_{1,i}$ for each β crosses the zero line at a critical R_3 , below and above which the perturbation is stable and unstable, respectively. The critical R_3 increases with decrease of β .

The neutral curve in the W_3 - β plane for $R_3 = 25$ is shown by the red lines in figure 11(a). As is illustrated in figure 9(b), for fixed R_3 and β , $\hat{c}_{1,i}$ may cross the zero line twice, provided that β is not too small. Consequently, the neutral curve exhibits a ‘banana’ shape, i.e. above a critical β , lower- and upper-branch neutral curves are observed. Inside the unstable zone, a blue line is plotted, which denotes the dispersion relation of the most unstable mode. These asymptotic predictions are compared favourably with the numerical

Asymptotic study of instability in a viscoelastic pipe

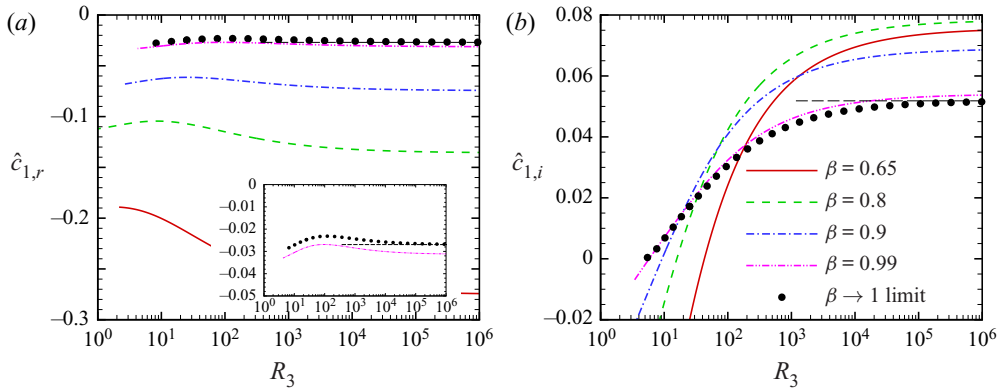


Figure 10. Dependence of the real (a) and imaginary (b) parts of \hat{c}_1 on R_3 in the short-wavelength regime, where $\bar{W}_3 = \sigma W_3 = 1.071$. The thin dashed lines represent the low-concentration prediction for $R_3 = \infty$. The inset in (a) shows a zoom-in plot for $-0.05 < \hat{c}_{1,r} < 0$.

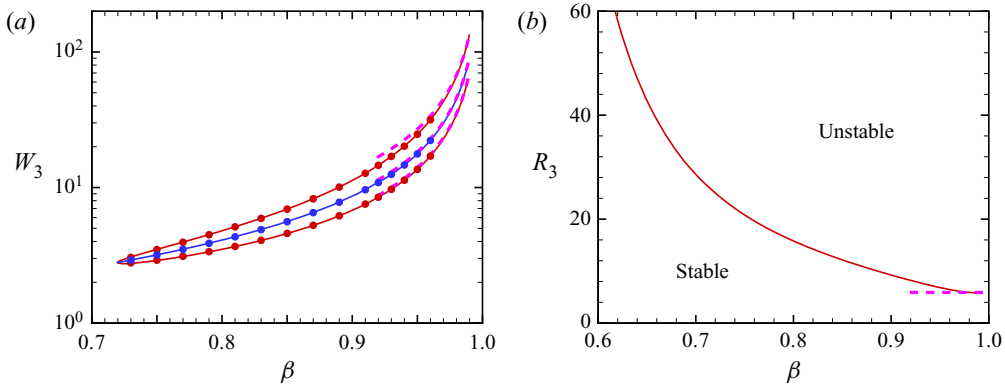


Figure 11. (a) The neutral (red) and the most unstable (blue) curves in the W_3 - β plane for $R_3 = 25$; (b) the neutral curve (red) in the R_3 - β plane for $\bar{W}_3 = 1.071$. The pink dashed lines represent the predictions in the low-concentration regime. The symbols in (a) are the EOS results for $k = 3$.

solutions of EOS for $k = 3$, shown by the red and blue circles in figure 11(a). As the wavenumber k decreases, the agreement becomes worse; however, this is not shown. As indicated by the black circles in figure 9, for $R_3 = 25$, the lower- and upper-branch neutral \bar{W}_3 appear at 0.71 and 1.35 (or $W_3 = 0.71\beta/(1 - \beta)$ and $W_3 = 1.35\beta/(1 - \beta)$), respectively, and the most unstable mode appears at $\bar{W}_3 = 0.91$ (or $W_3 = 0.91\beta/(1 - \beta)$). These values are shown by the dashed pink lines in figure 11(a). It is obvious that the red and blue solid lines approach the dashed pink lines consistently in the limit as $\beta \rightarrow 1$. In figure 11(b), we plot the neutral curve in the β - R_3 plane for a given $\bar{W}_3 = 1.071$. The stable and unstable zones are separated by the neutral curve, which approaches $R_3 = 5.9$, the low-concentration prediction.

For the low-concentration regime, the neutral curve can be plotted in the R_3 - \bar{W}_3 plane, which is shown in figure 12. As $R_3 \rightarrow \infty$, the neutral curve approaches a horizontal line, $\bar{W}_3 = 0.631$, which is predicted by the linear system (4.20) with R_3 being set to be ∞ . Above $\bar{W}_3 = 1.5$, there is another unstable zone, mode II, which will be shown in

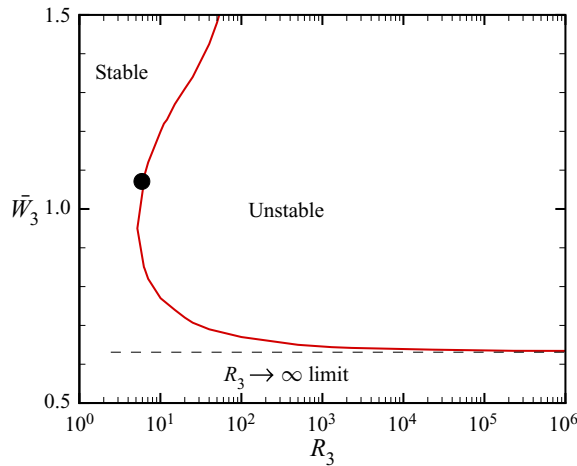


Figure 12. Neutral curve in the R_3 – \bar{W}_3 plane in the low-concentration short-wavelength regime, where the dashed line represents the prediction in the limit as $R_3 \rightarrow \infty$, and the filled circle indicates a representative neutral case, $(R_3, \bar{W}_3) = (5.9, 1.071)$.

figure 14. The filled circle denotes a representative case, $(R_3, \bar{W}_3) = (5.9, 1.071)$, which is also plotted by the pink dashed line in figure 11(b).

5.3. Comparison with the numerical solutions of Chaudhary et al. (2021)

In figure 21 of Chaudhary et al. (2021), the neutral curves in the Re – k plane were shown for small elasticity numbers, $E = Wi/Re$. Two representative β values, $\beta = 0.65$ and 0.9 , were selected for demonstration. For each fixed β , all the neutral curves collapse when Re , $1 - c$ and k are re-scaled by $Re E^{3/2}$, $(1 - c)/E$ and $kE^{1/2}$, respectively. In this subsection, we reproduce the collapsed neutral curves by the aforementioned asymptotic theories, explore more general scalings, and explain the reason behind these results.

According to (3.9a–c), the neutral curves of the lower and upper branches, in the limits $Re \gg 1$ and $k \leq O(1)$, can be described by

$$Re = \frac{\beta}{(W_1^{(1,3)})^2} k Wi^2. \tag{5.1}$$

Meanwhile, the phase-speed corrections of the two neutral modes, according to (3.10), are given by

$$c - 1 = \beta^{1/2} c_{1,r}^{(1,3)} k^{-1/2} Re^{-1/2}. \tag{5.2}$$

In order to reproduce figure 21 of Chaudhary et al. (2021), we re-express (5.1) and (5.2) as

$$Re E^{3/2} = \mathcal{A}_1 (kE^{1/2})^{-1} \quad \text{and} \quad (1 - c)/E = \mathcal{A}_2, \tag{5.3a,b}$$

where constants \mathcal{A}_1 and \mathcal{A}_2 are functions of only β , namely,

$$\mathcal{A}_1 = \frac{(W_1^{(1,3)})^2}{\beta}, \quad \mathcal{A}_2 = \frac{\beta c_{1,r}^{(1,3)}}{W_1^{(1,3)}}. \tag{5.4a,b}$$

It is interesting to notice that $(1 - c)/E$ is independent of $kE^{1/2}$, so the phase-speed correction $(1 - c)/E$ approaches a constant if assumptions (3.1) and (3.3) are satisfied.

Asymptotic study of instability in a viscoelastic pipe

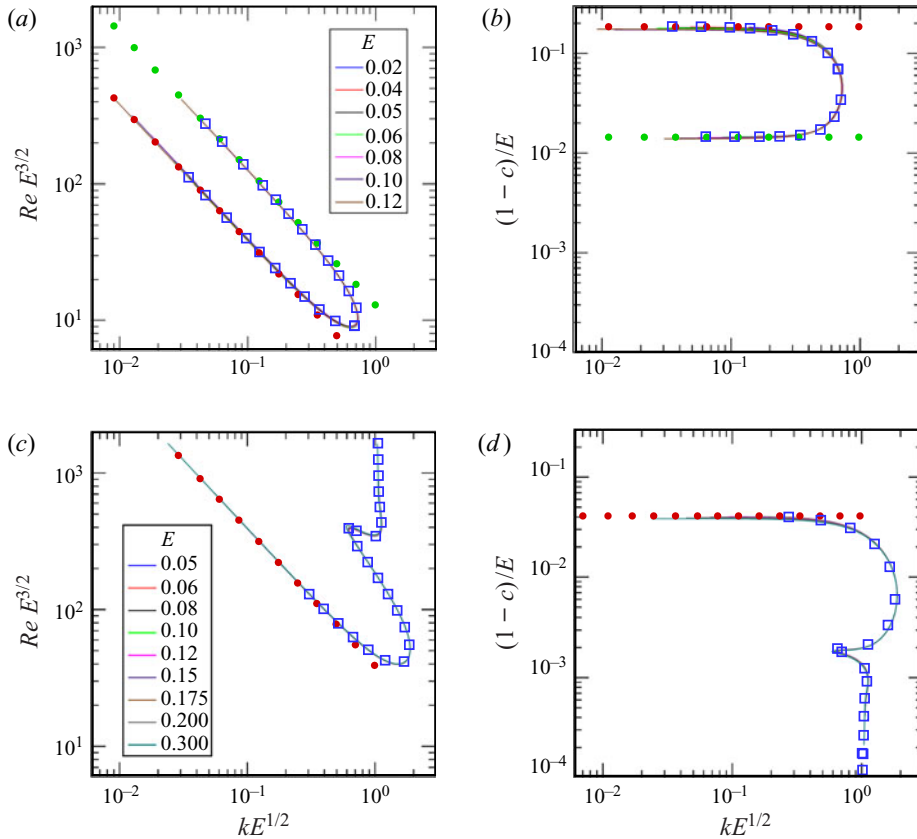


Figure 13. Comparisons between the asymptotic predictions and numerical results given by Chaudhary *et al.* (2021) (solid lines), where the red and green circles are the asymptotic predictions (5.3a,b) of the lower- and upper-branch neutral curves, respectively, and the blue squares are the asymptotic predictions from § 4.1. (a,b) $\beta = 0.65$, (c,d) $\beta = 0.9$.

For $\beta = 0.65$, only one group of unstable modes is observed from figures 6(a,b). It is obtained from table 2 that $(W_1^{(1)}, -c_{1,r}^{(1)}) \approx (1.56, 0.460)$ and $(W_1^{(3)}, -c_{1,r}^{(3)}) \approx (2.87, 0.0650)$. Therefore, for the two branches of neutral curves, $(\mathcal{A}_1, \mathcal{A}_2) \approx (3.75, 0.192)$ and $(12.7, 0.0147)$, respectively. For $\beta = 0.9$, two unstable modes appear, as shown in figures 6(c,d), and in the small wavenumber limit, only the instability mode includes the lower-branch neutral point, where $(W_1^{(0)}, -c_{1,r}^{(0)}) \approx (5.89, 0.270)$. Accordingly, the coefficients in (5.3a,b) are $(\mathcal{A}_1, \mathcal{A}_2) \approx (38.5, 0.041)$. The comparisons between the asymptotic predictions in the long-wavelength regime (filled circles) and the numerical solutions given by figures 21(a–d) of Chaudhary *et al.* (2021) are shown in figures 13(a–d). Perfect agreement is achieved in the limit $kE^{1/2} \ll 1$. It has to be mentioned that the choices of $kE^{1/2}$ and $Re E^{3/2}$ or $(1 - c)/E$ for collapse plotting are not unique, and more generic expressions for the dependence of control parameters for the neutral curves are (5.1) and (5.2), which are revealed by our analysis using the singular perturbation technique.

The long-wavelength asymptotic theory fails to predict the numerical results when $kE^{1/2} = O(1)$, for which k is large since a small E is assumed. Therefore, we apply the asymptotic theory for the short-wavelength regime. It is seen from § 4.1 that for a given β

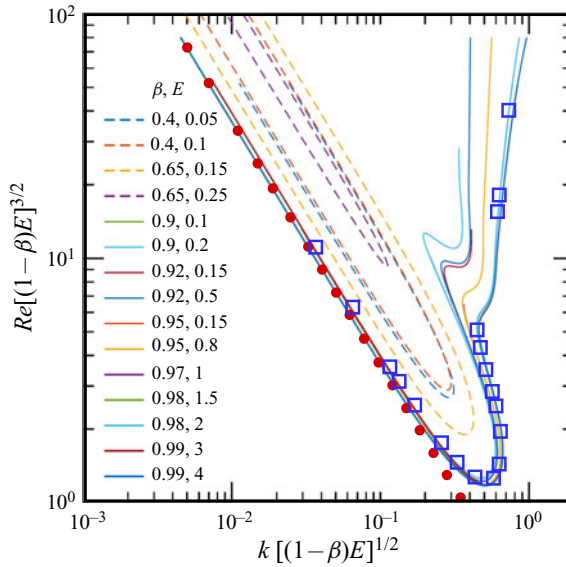


Figure 14. Neutral curves in the $k[(1-\beta)E]^{1/2}-Re[(1-\beta)E]^{3/2}$ plane. Solid lines, numerical results given by Chaudhary *et al.* (2021); red circles, asymptotic prediction from (5.6); blue squares, low-concentration asymptotic prediction.

that is of $O(1)$ but not close to unity, the instability is determined by R_3 and W_3 . They can be translated to $kE^{1/2}$, $Re E^{3/2}$ and $(1-c)/E$ via

$$kE^{1/2} = W_{3c}^{1/2} R_{3c}^{-1/4} \beta^{-1/2}, \quad Re E^{3/2} = W_{3c}^{3/2} R_{3c}^{1/4} \beta^{-1/2}, \quad (1-c)/E = \beta W_{3c}^{-1} \hat{c}_{1rc}, \tag{5.5a-c}$$

where the subscript c denotes the neutral value. For a given β , the neutral curve is uniquely determined in the $W_{3c}-R_{3c}$ plane. The values in (5.5a-c) are shown by the blue open squares in figure 13, which again agree well with the numerical solutions of Chaudhary *et al.* (2021). In the limit as $kE^{1/2} \rightarrow 0$, the short-wavelength predictions approach the long-wavelength predictions.

Figure 22 of Chaudhary *et al.* (2021) shows that the lower-branch neutral curves can also collapse in the low-concentration limit when plotting in the $Re[(1-\beta)E]^{3/2}-k[(1-\beta)E]^{1/2}$ plane. In the long-wavelength regime, it is readily seen from the lower pink dashed line in figure 6(a) that in the limit as $\beta \rightarrow 1$ or $\sigma \rightarrow 0$, the re-scaled Weissenberg number is inversely proportional to σ , namely, $W_1 = 0.6\sigma^{-1}$. Thus we obtain the relation

$$Re[(1-\beta)E]^{3/2} = \frac{0.36}{k[(1-\beta)E]^{1/2}}. \tag{5.6}$$

This relation is plotted by the red circles in figure 14, which shows good agreement with the lower-branch neutral modes given by figure 22 of Chaudhary *et al.* (2021) for $k[(1-\beta)E]^{1/2} \ll 1$. On the other hand, when $k[(1-\beta)E]^{1/2} = O(1)$, the short-wavelength regime is reached. The blue squares are re-scaled results of those in figure 12, with the mode II neutral curve added. The agreement between the numerical solutions of Chaudhary *et al.* (2021) as $\beta \rightarrow 1$ and the asymptotic prediction is again perfect.

Figures 24 and 25 of Chaudhary *et al.* (2021) show two different scalings for the collapse of the eigenfunctions. By looking at these figures, one may question why the

β	Re	k	$E \equiv Wi/Re$	Wi	$c_r - 1$	R_1	W_1	c_1
0.5	5000	1	0.0212	106	$-0.00516 + 0.000112i$	1000	1.06	$-0.516 + 0.0112i$
0.5	10000	1	0.0150	150	$-0.00368 + 0.000103i$	2000	1.06	$-0.520 + 0.0146i$
0.5	15000	1	0.0122	184	$-0.00302 + 0.000093i$	3000	1.06	$-0.522 + 0.0161i$
0.5	20000	1	0.0106	212	$-0.00262 + 0.000085i$	4000	1.06	$-0.523 + 0.0170i$

Table 3. Re-scale of the control parameters in figure 15.

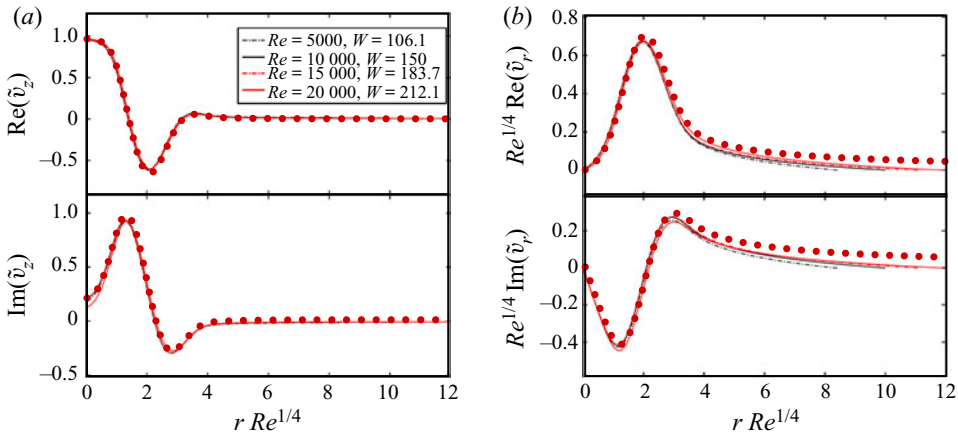


Figure 15. Eigenfunctions for a representative long-wavelength configuration, where the coloured lines are from figure 25 of Chaudhary *et al.* (2021), and the circles denote the asymptotic prediction given by § 3.1 with $W_1 = 1.06$.

eigenfunctions could agree with each other for a group of control parameters, but exhibit a different distribution for another group of control parameters. In the following, we will show an explanation by use of the asymptotic theories developed in this paper.

Let us first observe the parameters chosen for the plots. For figure 25 of Chaudhary *et al.* (2021), k is set to be 1, which satisfies the long-wavelength regime. Therefore, we calculate the re-scaled Reynolds number R_1 , Weissenberg number W_1 , and phase speed $c_1 = k^{1/2} R_1^{1/2} (c - 1)$ according to (3.9a–c) and (3.10), as shown in table 3. It is obvious that for $\beta = 0.5$, the linear system (3.25) is controlled only by W_1 , which is the same for all the selected cases. This is why their eigenfunctions collapse. In figure 15 we show the results of Chaudhary *et al.* (2021) by continuous curves, and also plot the eigenfunctions of the long-wavelength asymptotic mode with the same W_1 by the red circles, where the horizontal axis $r Re^{1/4}$ is translated to $k^{-1/4} \beta^{1/4} \tilde{y}$. As expected, the asymptotic predictions show good agreement with the numerical solutions, especially in the near-centre region. A slight discrepancy of the re-scaled \hat{v}_r in the region where $r Re^{1/4} \in (4, 12)$ is attributed to the finite- Re effect. Of course, if we choose another group of control parameters for which W_1 is different, then the eigenfunctions must be different from those in figure 15, but as long as $k \leq O(1)$, the central-layer scaling $r \sim Re^{-1/4}$ still works. These can be understood only by the asymptotic analysis. Also, the asymptotic analysis suggests that the re-scaled phase-speed correction for $(\beta, W_1) = (0.5, 1.06)$ is $-0.522 + 0.0289i$, which is the large- Re asymptote of the numerical solutions.

β	Re	k	$E \equiv Wi/Re$	Wi	$c_r - 1$	R_3	W_3	\hat{c}_1
0.4	1962	2.713	0.020	39.2	-0.00329	245	0.923	-0.380
0.4	1410	2.423	0.025	35.3	-0.00409	248	0.924	-0.378
0.4	1078	2.207	0.030	32.3	-0.00487	251	0.926	-0.376
0.4	861	2.037	0.035	30.1	-0.00563	255	0.927	-0.373
0.4	710	1.898	0.040	28.4	-0.00638	260	0.929	-0.370

Table 4. Re-scale of the control parameters in figure 16.

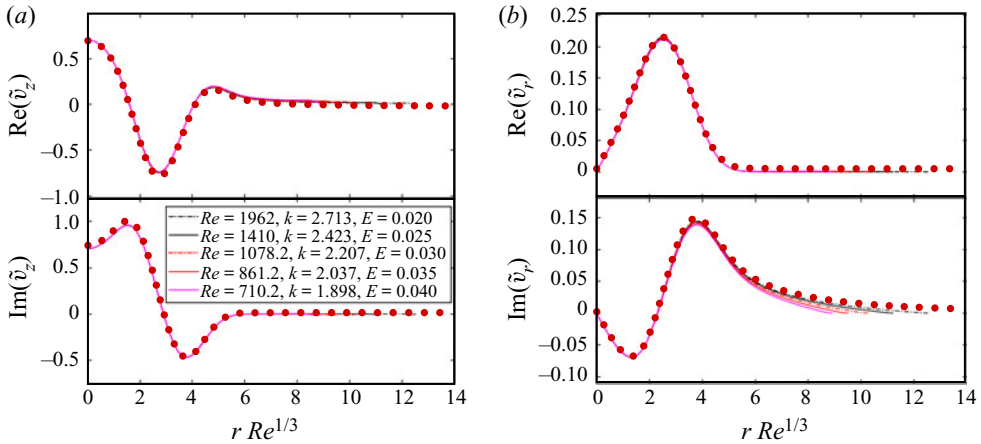


Figure 16. Eigenfunctions for a representative short-wavelength configuration, where the coloured lines are from figure 24 of Chaudhary *et al.* (2021), and the circles denote the asymptotic prediction given by § 4.1 with $W_3 = 0.925$ and $R_3 = 245$.

Figure 24 of Chaudhary *et al.* (2021) shows an alternative scaling for which the eigenfunctions for another group of control parameters collapse. Since the selected k for each case is greater than unity, we compare the results with the short-wavelength predictions. For a fixed β , the control parameters in the short-wavelength regime are R_3 and W_3 , which are converted from Re , E and k via (4.2a–c). As shown in table 4, R_3 and W_3 for all the selected cases are almost the same, leading to agreements of the eigenvalue \hat{c}_1 and the eigenfunctions between the numerical solutions and the asymptotic predictions; see figure 16.

6. Concluding remarks

The transition to turbulence in a Newtonian pipe flow can happen only in subcritical conditions; however, a supercritical route is possible when the pipe flow is viscoelastic, as was found first by Garg *et al.* (2018) based on the Oldroyd-B model. A systematic numerical study of linear viscoelastic instability was provided subsequently by Chaudhary *et al.* (2021). Because viscoelastic instability depends on more control parameters (Re , Wi , β and k for the axisymmetric mode) than the Newtonian instability does, the numerical results of the former appear to be quite complicated and are difficult to present in a well-organised manner. Therefore, in this paper we revisit the Oldroyd-B viscoelastic instability problem by employing the singular perturbation (asymptotic) technique, to reveal the intrinsic mechanism and the relevant controlling ‘similarity parameters’

(combination of Re , Wi , β and k) of the centre instability emerging in the viscoelastic pipe flow.

Taking Re to be asymptotically large, two regimes relating to the viscoelastic instability emerge, both of which have phase speeds rather close to the centreline velocity, and so are referred to as the centre modes. For each regime, the instability exhibits a three-layered structure in the radial direction from the wall to the centreline – a passive wall (Stokes) layer, a main layer and a central layer – but the thicknesses of the central layers for the two regimes are of different scalings depending on the parameters.

- (i) The first regime is the long-wavelength centre instability, for which the wavenumber $k \ll 1$. It must be noted that this instability is also applicable to that for $k = O(1)$, but for convenience we still call this mode ‘long wavelength’. For a regular β that is not close to unity, the thickness of the central layer for this regime is $r \sim k^{-1/4} Re^{-1/4}$, and its scaled phase-speed correction $k^{1/2} R_1^{1/2} (c_r - 1)$ and growth rate $k^{1/2} R_1^{1/2} c_i$ for a given β depend only on a combined parameter $W_1 = k^{1/2} R_1^{1/2} Wi$, where $R_1 = Re/\beta$. Such an observation reduces the complexity of the original instability system remarkably. In the most distinguished layer (central), the instability is driven by balance of the inertia, pressure gradient, viscosity and polymer stress, all of which play a dominant role. A single unstable zone (mode I) is observed when $\beta < 0.8$, but an additional one (mode II) emerges for higher β values. The two unstable zones merge when $\beta \approx 0.88$, and the upper-branch neutral curve of mode II approaches infinity as $\beta \rightarrow 0.88$. A salient nature of the mode II instability is its connection to the high- W_1 behaviour. For $W_1 \gg 1$, the dominant factors in the central layer are redistributed in three sublayers: the balance of the inertia and pressure gradient dominates the bulk central layer, that of the inertia and polymer stress dominates the outer central layer, and that of the viscosity and polymer stress dominates the core central layer. W_1 of the unstable zones increases with β monotonically. In the low-concentration limit, as $\beta \rightarrow 1$, W_1 becomes inversely proportional to $1 - \beta$, as shown analytically and numerically in § 3.2 and figure 6, respectively.
- (ii) The second regime is the short-wavelength centre instability, with $k \gg 1$. The main-layer solution for this regime is of the WKB form, which is in contrast to the algebraic form for $k \ll 1$ and the Bessel-function form for $k = O(1)$. More importantly, the central-layer thickness is changed to $r \sim k^{-1} \sim Re^{-1/3}$, leading to a scaling law different from regime (i). The instability mechanism is also the balance of the inertia, pressure gradient, viscosity and polymer stress terms in the central layer. The dispersion relation of the short-wavelength mode for a given regular β is dependent on two parameters, R_3 and W_3 , and when $R_3 \rightarrow \infty$, this regime approaches regime(i). For a relatively small R_3 , there exists only one unstable zone, and again, as $\beta \rightarrow 1$, W_3 of the unstable modes increases inversely with $1 - \beta$, which is demonstrated analytically in § 4.2 and numerically in figure 11.

Additionally, in the limit as $\beta \rightarrow 1$, a critical layer, with thickness $O(\sigma k^{-1/4} Re^{-1/4})$ for the long-wavelength regime or $O(\sigma k^{-1})$ for the short-wavelength regime, may emerge in the central layer when the centre mode is neutral to leading-order accuracy, as sketched in figure 2. As the outer solutions approach the critical layer, \hat{v}_r remains regular, but its derivative with respect to r and \hat{u}_z is associated with logarithmic singularities. The latter is removed when the viscosity is taken into account in the thin critical layer; see Appendix C.

The asymptotic predictions are verified by solving directly the complete linearised equations using a spectral collocation method, and good agreement is achieved especially

when the Reynolds number is sufficiently large and the wavenumber satisfies $k \leq O(1)$ for regime(i), and k is sufficiently large (the Reynolds number is also large as $Re \propto k^3$) for regime(ii). Also, we have compared our asymptotic predictions with the numerical results of the neutral curves and eigenfunctions given by Chaudhary *et al.* (2021). In the latter paper, the neutral curves for a given β that is not close to unity collapse when Re , $1 - c$ and k are re-scaled by certain powers of E , and those in the limit as $\beta \rightarrow 1$ collapse when Re and k are re-scaled by the same powers of $(1 - \beta)E$. Such observations are quite empirical, but lack *a priori* analysis to shed light on the instability mechanism. From our asymptotic analysis, it is found that for a fixed β , the neutral curves of the long-wavelength centre modes depend only on a single combined parameter W_1 , whereas those of the short-wavelength modes depend on R_3 and W_3 . The collapse by the re-scaling of the control parameters is a reflection of the asymptotic findings. Moreover, the asymptotic analysis implies that there could be more re-scaling strategies that lead to neutral curve collapse. Additionally, the eigenfunctions can collapse in two different radial scalings, $r Re^{1/4}$ and $r Re^{1/3}$, but it was not clear from Chaudhary *et al.* (2021) which scaling should be used for an arbitrarily chosen parameter group. Such a phenomenon can be explained readily by our asymptotic analysis: namely, the two scalings correspond to the central-layer thicknesses of the long- and short-wavelength regimes, respectively.

Finally, we mention that our asymptotic work can be extended readily to further investigations. A recent weakly nonlinear analysis of a viscoelastic pipe flow (Wan *et al.* 2021) shows that for $Wi \gg 1$, the Landau coefficient (in the Ginzburg–Landau equation) satisfies a certain scaling law when plotting against β . Actually, such a scaling law can be explained using the long-wavelength asymptotic system (3.26), which will be reported in a future work.

Acknowledgements. M.D. is supported by the National Science Foundation of China (grant nos 11988102, U20B2003, 11772224), and M.Z. is supported by the Ministry of Education, Singapore (a Tier 2 grant with the WBS no. R-265-000-661-112).

Declaration of interests. The authors report no conflict of interest.

Author ORCIDs.

 Ming Dong <https://orcid.org/0000-0003-3408-8613>;

 Mengqi Zhang <https://orcid.org/0000-0002-8354-7129>.

Appendix A. Numerical method for the linear stability code and its verification

A linear stability code solving the 3-D linearised equations (2.3) has been implemented by use of the Petrov–Galerkin (PG) method (Meseguer & Trefethen 2003). In this method, pressure is eliminated because a solenoidal base (which automatically satisfies the continuity equation) is used for the velocity field. At the wall where $r = 1$, the no-slip, non-penetration boundary conditions are applied for the velocity field, but we do not need to impose a boundary condition for the conformation tensor. At the centreline, $r = 0$, we avoid placing a grid point there following Mohseni & Colonius (2000), and the derivative matrices are constructed following Trefethen (2000), exploiting the odd/even property of each variable. In this implementation, there is no need to consider regularity conditions around $r = 0$ according to Mohseni & Colonius (2000).

The eigenspectrum for a Newtonian pipe flow ($\beta = 1$, and the viscoelastic equations are discarded) with $Re = 5000$ is shown by the red dots in figure 17(a). There exist only discrete modes for which the eigenvalues appear as discrete points, and the spectrum exhibits a ‘Y’ shape. Following the study for plane Poiseuille flows (Mack 1976), these

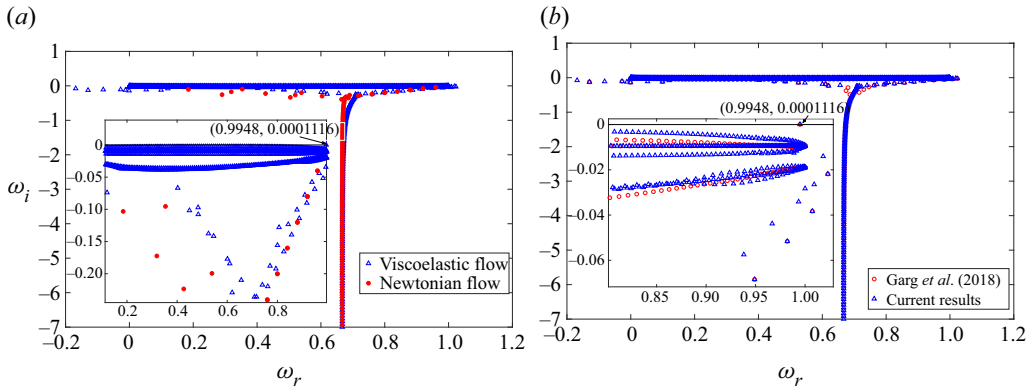


Figure 17. (a) Comparison of the eigenspectra between a viscoelastic pipe flow ($Re = 5000$, $Wi = 106.1$, $\beta = 0.5$, $k = 1$) and a Newtonian pipe flow ($Re = 5000$, $\beta = 1$, $k = 1$). (b) Comparison of the viscoelastic eigenspectra between our results and those in Garg *et al.* (2018), where the parameters are the same as the blue triangles in (a). The unstable centre viscoelastic modes are marked in both panels.

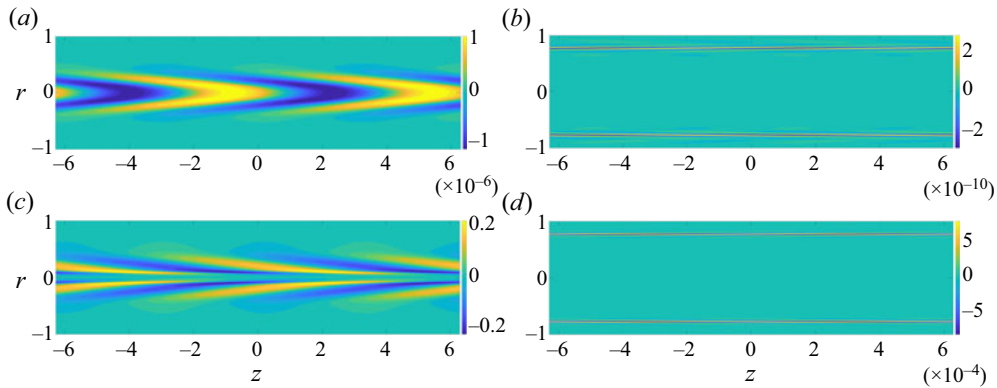


Figure 18. Contours of the perturbations \hat{u}_z (a,b) and \hat{c}_{11} (c,d) of the centre (a,c) and wall (b,d) modes for $Re = 5000$, $Wi = 106.1$, $\beta = 0.5$, $k = 1$. The complex eigenvalues for the centre and wall modes are $\omega = 0.9948 + 0.0001116i$ and $0.4024 - 0.06671i$, respectively.

discrete modes can be classified by three branches: A ($c_r \rightarrow 0$), P ($c_r \rightarrow 1$) and S ($c_r \approx 2/3$). The former two are also referred to as the wall mode and centre mode, respectively. In plane Poiseuille flows, the wall mode can become unstable when the Reynolds number is sufficiently high, whereas for Newtonian pipe flows, all these modes are stable for all Reynolds numbers. However, Newtonian pipe flows at this Re can become turbulent, indicating a subcritical transition scenario. On the other hand, as reviewed in § 1, the centre mode can become unstable in viscoelastic pipe flows, as exemplified by the blue triangles in figure 17(a). The complex eigenvalue $\omega = 0.9948 + 0.0001116i$ of the only unstable centre mode in this panel is marked in the inset figure. The contours of the perturbation eigenfunctions, \hat{u}_z and \hat{c}_{11} , for a typical wall mode ($\omega = 0.4024 - 0.06671i$) and the unstable centre mode are compared in figure 18. The perturbations of the centre mode are concentrated around the centreline, showing a chevron-shaped structure similar to the experimental observation of the onset of elastoinertial instability in viscoelastic pipe flows (Choueiri *et al.* 2021). This structure is in contrast to that of the wall mode, in which the perturbations peak in a thin layer close to the wall.

A detailed comparison of the eigenspectra obtained by our code with those of Garg *et al.* (2018) is shown in figure 17(b). Because our code is 3-D, in contrast to the 2-D (axisymmetric) code of Garg *et al.* (2018), we have obtained more modes than theirs, but the overall agreement between the two families of eigenspectra is good. A more detailed validation step can be found in Zhang (2021).

Appendix B. Centre modes for $k = O(1)$

Although the analysis in § 3 is based on $k \ll 1$, we will show that the regime also applies when the wavelength is comparable to the pipe radius, $k = O(1)$. Here we show only the asymptotic analysis for a regular-level concentration $(\beta, 1 - \beta) = O(1)$; that for a low-level concentration, $0 < 1 - \beta \ll 1$, follows the same procedure.

The centre mode for $k = O(1)$ exhibits the same asymptotic structure as in figure 2. Following the same procedure as in § 3, we introduce a group of $O(1)$ parameters

$$\tilde{W}_1 = R_1^{-1/2} Wi, \quad \tilde{W}_2 = \beta \tilde{W}_1 / (1 - \beta), \tag{B1a,b}$$

and expand the complex phase speed as

$$c = 1 + R_1^{-1/2} \tilde{c}_1 + O(R_1^{-1}). \tag{B2}$$

B.1. Main-layer solution

The perturbation field in this regime is expressed in terms of asymptotic series

$$(\hat{u}_z, \hat{u}_r, \hat{p}) = (\bar{u}_0, \bar{v}_0, \bar{p}_0) + R_1^{-1/2} (\bar{u}_1, \bar{v}_1, \bar{p}_1) + \dots, \tag{B3a}$$

$$(\hat{c}_{11}, \hat{c}_{12}, \hat{c}_{22}) = (R_1 \bar{c}_{11,0}, R_1 \bar{c}_{12,0}, R_1^{1/2} \bar{c}_{22,0}) + \dots. \tag{B3b}$$

Substituting (B3) into (2.6) and retaining the leading-order terms, we obtain

$$r^2 \left(\frac{d^2}{dr^2} - \frac{d}{r dr} - k^2 \right) (r \bar{v}_0) = 0, \tag{B4}$$

whose general solution is

$$\bar{v}_0 = A_3 I_1(kr) + A_4 K_1(kr), \tag{B5}$$

where I_1 and K_1 are the modified Bessel functions of the first and second kinds, respectively, and A_3 and A_4 are constants to be determined. Being similar to § 3.1.1, the boundary condition at the wall, $\bar{v}_0(1) = 0$, has to be imposed, and therefore we obtain $A_4/A_3 = -I_1(k)/K_1(k)$. Substituting into the continuity and axial-momentum equations, we obtain

$$\bar{u}_0 = \frac{i}{k} \left(\bar{v}'_0 + \frac{\bar{v}_0}{r} \right), \quad \bar{p}_0 = \frac{ir}{k} (-\bar{v}_0 + r \bar{v}'_0). \tag{B6a,b}$$

Near the centreline, the hydrodynamic perturbations behave as

$$(\bar{u}_0, \bar{v}_0, \bar{p}_0) \rightarrow A_4 \left(i \ln(kr), \frac{1}{kr}, -\frac{2i}{k^2} \right) + \dots \quad \text{as } r \rightarrow 0. \tag{B7}$$

For normalisation, we take $\bar{p}_0(0) = 1$, and therefore

$$(A_3, A_4) = \left(-\frac{ik^2 K_1(k)}{2I_1(k)}, \frac{ik^2}{2} \right). \tag{B8}$$

The leading-order conformation tensor perturbations are governed by equations similar to (3.14), but with a prefactor k appearing in the first and fourth terms of (3.14a). The solutions are

$$\bar{c}_{11,0} = -\frac{16i\tilde{W}_1^2}{k}\bar{v}'_0, \quad \bar{c}_{12,0} = -8\tilde{W}_1^2\bar{v}_0, \quad \bar{c}_{22,0} = \frac{4\tilde{W}_1}{r}\bar{v}_0. \tag{B9a-c}$$

The solution for the second-order perturbation \bar{v}_1 is

$$\begin{aligned} \bar{v}_1 = & 16\tilde{W}_1^2\tilde{W}_2^{-1} \int_1^r [I_1(kr) K_1(kt) - I_1(kt) K_1(kr)] \left[\frac{\bar{v}_0(t)}{t^3} - \frac{\bar{v}'_0(t)}{t^2} \right] dt \\ & + A_5 I_1(kr) + A_6 K_1(kr), \end{aligned} \tag{B10}$$

where the constants A_5 and A_6 are related by $A_6 = -I_1(k)/K_1(k)A_5$ from the non-penetration boundary condition. Therefore, in the limit as $r \rightarrow 0$, the radial velocity behaves like

$$\hat{u}_r \rightarrow A_4 \left[\frac{1}{kr} + \dots + R_1^{-1/2} \left(\frac{4\tilde{W}_1^2\tilde{W}_2^{-1}}{kr^3} + \dots \right) \right]. \tag{B11}$$

Obviously, this asymptotic expression ceases to be valid when $r \sim R_1^{-1/4}$, and again, a central layer needs to be taken into account.

B.2. Central-layer solution

For convenience, we introduce an $O(1)$ coordinate

$$Y = R_1^{1/4}r, \tag{B12}$$

and the perturbation field is expanded as

$$(\hat{v}_z, \hat{v}_r, \hat{p}, \hat{c}_{11}, \hat{c}_{12}, \hat{c}_{22}) = (R_1^{1/2}\check{u}, R_1^{1/4}\check{v}, \check{p}, R_1^{3/2}\check{c}_{11}, R_1^{5/4}\check{c}_{12}, R_1\check{c}_{22}) + \dots \tag{B13}$$

The governing equations are obtained by substituting (B13) into (2.6), to give

$$\frac{d\check{\phi}}{dY} = \check{L}\check{\phi}, \tag{B14}$$

where $\check{\phi} = (\check{u}, \check{u}', \check{u}'', \check{v})^T$ and the non-zero elements of \check{L} are

$$\check{L}_{12} = 1, \quad \check{L}_{23} = 1, \quad \check{L}_{31} = \frac{16k^4\tilde{W}_1^2Y(Y^4 - \check{c}_1^2)}{\check{L}^2(1 + \tilde{W}_2\check{L})}, \quad \check{L}_{41} = -ik, \quad \check{L}_{44} = -1/Y, \tag{B15}$$

$$\begin{aligned} \check{L}_{32} = & \frac{8k^2Y^4 - 8kY^2(i + 2k\tilde{W}_1Y^2)\check{L} + (1 + 8ik\tilde{W}_1Y^2 + 8k^2\tilde{W}_1^2Y^4)\check{L}^2}{Y^2\check{L}^2(1 + \tilde{W}_2\check{L})} \\ & + \frac{\tilde{W}_2(1 - ikY^2(Y^2 + \check{c}_1))\check{L}^3}{Y^2\check{L}^2(1 + \tilde{W}_2\check{L})}, \end{aligned} \tag{B16}$$

$$\check{L}_{33} = -\frac{-4ikY^2 + \check{L} - 4ik\tilde{W}_1Y^2\check{L} + \tilde{W}_2\check{L}^2}{Y\check{L}(1 + \tilde{W}_2\check{L})}, \quad \check{L}_{34} = -\frac{32ik^3\tilde{W}_1^2Y^2(Y^2 - \check{c}_1)}{\check{L}^2(1 + \tilde{W}_2\check{L})}, \tag{B17a,b}$$

with $\check{L} = ik(-Y^2 - \check{c}_1) + \check{W}_1^{-1}$. The boundary conditions (3.31) and (3.32) are still valid.

Comparing with the linear system (3.26), we find that they are exactly the same if $(\check{W}_1, \check{W}_2, \check{L}, k)$ in (3.26) is replaced by $(W_1, W_2, \check{L}, 1)$. The implication is that the long-wavelength instability regime analysed in § 3 is also valid for $k = O(1)$, but in this paper, this mode is referred to as the long-wavelength centre mode for brevity.

Appendix C. Critical-layer analysis for the long-wavelength neutral instability in the low-concentration limit

The linear system (3.38), governing the low-concentration long-wavelength instability introduced in § 3.2, may become singular when $\bar{c}_{1,i} = 0$, so a critical layer appearing at

$$\check{y}_c = \sqrt{-\bar{c}_1} \tag{C1}$$

must be taken into account. For the phase-speed expansion (3.35), \bar{c}_2 is taken to be of $O(1)$.

According to (3.38) and (3.41), the central-layer perturbation field in the limit as $\check{y} \rightarrow \check{y}_c$ behaves like

$$\check{U}_0 \rightarrow i\mathcal{C}_1 \ln(\check{y} - \check{y}_c) + i\mathcal{C}_1 + \frac{i\mathcal{C}_0}{\check{y}_c} + \frac{i\mathcal{C}_1(\check{y} - \check{y}_c) \ln(\check{y} - \check{y}_c)}{\check{y}_c} + \dots, \tag{C2a}$$

$$\check{V}_0 \rightarrow \mathcal{C}_0 + \mathcal{C}_1(\check{y} - \check{y}_c) \ln(\check{y} - \check{y}_c) + \dots, \tag{C2b}$$

$$\check{U}_1 \rightarrow -\frac{2(i + \bar{W}\bar{c}_2)\mathcal{C}_0}{(\check{y} - \check{y}_c)} + \dots, \quad \check{V}_1 \rightarrow 2(i\bar{W}\bar{c}_2 - 1)\mathcal{C}_0 \ln(\check{y} - \check{y}_c) + \dots, \tag{C2c,d}$$

where \mathcal{C}_0 and \mathcal{C}_1 are constants, and $\mathcal{C}_1 = 4i\bar{W}\check{y}_c\mathcal{C}_0$. The second-order terms become comparable to the leading-order ones when $\check{y} - \check{y}_c \sim \sigma$, and therefore the thickness of the critical layer is found to be of $O(\sigma)$. For convenience, we introduce a local coordinate

$$\eta = \sigma^{-1}(\check{y} - \check{y}_c). \tag{C3}$$

The leading-order perturbations in the critical layer are expanded as

$$(\hat{v}_z, \hat{v}_r, \hat{p}) = \hat{p}_0[k^{1/2}R_1^{1/2}\check{U}, k^{5/4}R_1^{1/4}(\mathcal{C}_0 + \sigma\bar{V}), 1] + \dots, \tag{C4a}$$

$$(\hat{c}_{11}, \hat{c}_{12}, \hat{c}_{22}) = \hat{p}_0(k^{-1/2}R_1^{3/2}\sigma^{-4}\bar{C}_{11}, k^{1/4}R_1^{5/4}\sigma^{-3}\bar{C}_{12}, kR_1\sigma^{-2}\bar{C}_{22}) + \dots. \tag{C4b}$$

They are governed by

$$i\bar{U} + \bar{V}' + \mathcal{C}_0/\check{y}_c = 0, \quad \bar{U}'' + \bar{W}^{-1}(i\bar{C}_{11} + \bar{C}'_{12}) = 0, \tag{C5a,b}$$

$$\check{L}_2\bar{C}_{11} = -4\check{y}_c\bar{C}_{12}, \quad \check{L}_2\bar{C}_{12} = 8i\check{y}_c^2\bar{W}^2\mathcal{C}_0 - 2\check{y}_c\bar{C}_{22}, \quad \check{L}_2\bar{C}_{22} = -4i\bar{W}\check{y}_c\mathcal{C}_0, \tag{C5c-e}$$

where $\check{L}_2 = -2i\check{y}_c\eta - i\bar{c}_2 + \bar{W}^{-1}$. The solutions to the above system are

$$\bar{U} = -4\bar{W}\check{y}_c\mathcal{C}_0 \ln(i\bar{W}\check{L}_2) + \mathcal{C}_4 + 2\mathcal{C}_5\eta, \tag{C6a}$$

$$\begin{aligned} \bar{V} = 4i\bar{W}\check{y}_c\mathcal{C}_0 & \left[-\frac{(-\bar{W}^{-1} + i\bar{c}_2) \tan^{-1}[\bar{W}(2\check{y}_c\eta + \bar{c}_2)]}{2\check{y}_c} + \eta \ln(i\bar{W}\check{L}_2) \right] \\ & + (i\bar{c}_2\bar{W} - 1) \ln[1 + \bar{W}^2(2\check{y}_c\eta + \bar{c}_2)^2]\mathcal{C}_0 + \mathcal{C}_3 \\ & + \left(-i\mathcal{C}_4 - \frac{\mathcal{C}_0}{\check{y}_c} - 4i\bar{W}\check{y}_c\mathcal{C}_0 \right) \eta - i\mathcal{C}_5\eta^2. \end{aligned} \tag{C6b}$$

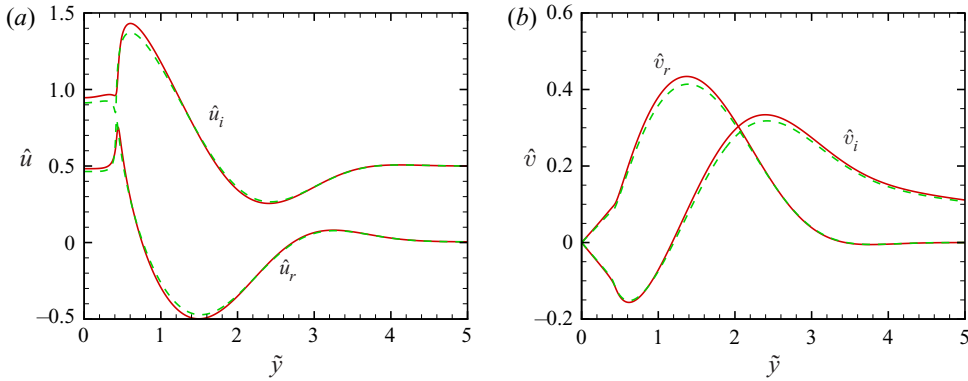


Figure 19. Eigenfunctions of \hat{u} and \hat{v} for a near-neutral low-concentration mode. (a) Solution from § 3.1 with $\beta = 0.99$, $W_1 = 63$ and $\bar{c}_1 = -0.183 + 0.004i$; (b) solution from § 3.2 with $\bar{W} = 0.64$ and $\bar{c}_1 = -0.172 + 0.004i$.

As $\eta \rightarrow \pm\infty$,

$$\bar{U} \rightarrow -4\bar{W}\bar{y}_c\mathcal{C}_0 \ln(2\bar{W}\bar{y}_c\eta) - \frac{2\mathcal{C}_0(i + \bar{W}\bar{c}_2)}{\eta} + \mathcal{C}_4 + 2\mathcal{C}_5\eta + \dots, \quad (C7a)$$

$$\bar{V} \rightarrow 4i\bar{W}\bar{y}_c\mathcal{C}_0\eta \ln(2\bar{W}\bar{y}_c\eta) + 2(\bar{W}\bar{c}_2i - 1) \ln \eta \mathcal{C}_0 + \left(-i\mathcal{C}_4 - \frac{\mathcal{C}_0}{\bar{y}_c} - 4i\bar{W}\bar{y}_c\mathcal{C}_0\right)\eta - i\mathcal{C}_5\eta^2. \quad (C7b)$$

Apparently, there is a phase jump from $\eta = -\infty$ to $\eta = \infty$ due to the logarithmic term $\ln \eta$, similar to the classical critical-layer analysis in Drazin & Reid (2004). Matching with the central-layer solution, we obtain

$$\mathcal{C}_5 = 0, \quad \mathcal{C}_4 = \left(\frac{i}{\bar{y}_c} - 4\bar{W}\bar{y}_c + 4\bar{W}\bar{y}_c \ln(2\bar{W}\bar{y}_c)\right)\mathcal{C}_0. \quad (C8a,b)$$

Figure 19 plots the eigenfunctions of the quasi- lower-branch neutral mode in the low-concentration limit. The solutions from § 3.1 with $\beta = 0.99$ and from § 3.2 agree with each other well. An enlargement of \hat{u} at around $\tilde{y} = 0.44$ is observed, which agrees with the critical-layer analysis, and the location of the critical layer is $\tilde{y}_c = \sqrt{-c_1} \approx 0.43$. The \hat{v} -eigenfunction stays finite at the critical position, but the derivative of \hat{v} with respect to \tilde{y} is large due to its logarithmic asymptote; see (C2d).

Appendix D. Large- W_1 analysis of mode II in the long-wavelength regime

As shown in figure 6(a), W_1 of the upper-branch neutral point of mode II approaches infinity for β close to unity, and the asymptotic behaviour of the mode II instability in the limit as $W_1 \rightarrow \infty$ is analysed in this appendix. In such a limit, the complex phase speed c_1 becomes small with a scaling $c_1 \sim W_1^{-1}$, so we introduce

$$c_1^\dagger = W_1 c_1. \quad (D1)$$

Additionally, the central layer in this limit splits into three asymptotic sublayers: the core central layer where $\tilde{y} = O(W_1^{-1/2})$, the bulk central layer where $\tilde{y} = O(1)$, and the outer central layer where $\tilde{y} = O(W_1^{1/2})$, respectively.

D.1. Bulk central layer

In this layer, we expand the solution in terms of an asymptotic series $(\tilde{u}, \tilde{v}) = (\tilde{u}_0, \tilde{v}_0) + W_1^{-1}(\tilde{u}_1, \tilde{v}_1) + O(W_1^{-2})$. Substituting this expansion into the governing equation system (3.26) and collecting the terms up to the first two orders, we obtain the solutions (the mathematical details are omitted for brevity)

$$\tilde{u} = 2i\tilde{C}_1 + i\tilde{C}_2(1 + 2 \ln \tilde{y}) + W_1^{-1} \frac{i\tilde{C}_2\tilde{y}^2}{4} + \dots, \tag{D2a}$$

$$\tilde{v} = \tilde{C}_1\tilde{y} + \tilde{C}_2\tilde{y} \ln \tilde{y} + W_1^{-1} \frac{\tilde{C}_2\tilde{y}^2}{16} + \dots, \tag{D2b}$$

where \tilde{C}_1 and \tilde{C}_2 are constants. It is found that the leading-order balance in this layer is between inertia and pressure gradient, rendering an inviscid nature.

However, in the limit as $\tilde{y} \rightarrow \infty$, the $O(W_1^{-1})$ term may be comparable with the leading-order solution, leading to the emergence of the outer central layer.

D.2. Outer central layer

In this layer, we introduce a local coordinate $\tilde{y}_1 = W_1^{-1/2}\tilde{y} = O(1)$, and the radial velocity \tilde{v} is of $O(W_1^{-1/2}\tilde{u})$ to leading order. The leading-order balance is between inertia and polymer stress. Solving the leading-order equations with the matching conditions of the core central layer being considered, we obtain

$$\tilde{u} = \frac{i[16\tilde{C}_1 - 2\tilde{C}_2 \ln \tilde{y}_1 + \tilde{C}_2 \ln(\tilde{y}_1^2 - 8)]}{8} + \frac{i\tilde{C}_2}{\tilde{y}_1^2 - 8} + \dots, \tag{D3a}$$

$$\tilde{v} = W_1^{-1/2} \frac{\tilde{y}[16\tilde{C}_1 - 2\tilde{C}_2 \ln \tilde{y}_1 + \tilde{C}_2 \ln(\tilde{y}_1^2 - 8)]}{16} + \dots. \tag{D3b}$$

It is easy to see that $(\tilde{u}', \tilde{u}'') \rightarrow 0$ as $\tilde{y}_1 \rightarrow \infty$, satisfying the boundary conditions (3.31).

D.3. Core central layer

Taking the lower limit of (D2), we find that the no-slip condition is not satisfied, although the non-penetration condition is satisfied. Therefore, a core central layer must be considered. By balance of the inertia terms, we can estimate that the thickness of the core central layer is of $O(W_1^{-1/2})$. Thus the local coordinate

$$\tilde{y}_2 = W_1^{1/2}\tilde{y} \tag{D4}$$

is introduced.

The leading-order balance of the momentum equation is between only viscosity and polymer stress, and the governing equation can be expressed in the same form as (3.26), but with $(\tilde{y}, W_1, W_2, \tilde{L})$ being replaced by $(\tilde{y}_2, 1, \sigma^{-1} \equiv \beta/(1 - \beta), \tilde{L}^\dagger \equiv -i(\tilde{y}_2^2 + c_1^\dagger) + 1)$,

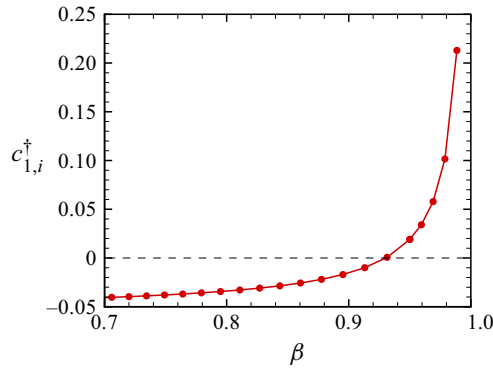


Figure 20. Dependence of the growth rate on β for the large- W_1 mode II instability.

and \tilde{L}_{32} being replaced by

$$\frac{8\tilde{y}_2^4 - 8\tilde{y}_2^2(i + 2\tilde{y}_2^2)\tilde{L}^\dagger + (1 + 8i\tilde{y}_2^2 + 8\tilde{y}_2^4)(\tilde{L}^\dagger)^2 + \sigma^{-1}(\tilde{L}^\dagger)^3}{\tilde{y}_2^2(\tilde{L}^\dagger)^2(1 + \sigma^{-1}\tilde{L}^\dagger)}. \tag{D5}$$

The boundary conditions at the centreline are also (3.32), whereas matching with the bulk central layer, we obtain $(\tilde{u}', \tilde{u}'') \rightarrow 0$ as $\tilde{y}_2 \rightarrow \infty$. Such a system can be solved by the same numerical approach as in §§ 3 and 4.

D.4. Numerical results for the large- W_1 mode II instability

The system in § D.3 is so simple that there is only one control parameter, β . The dependence of the growth rate c_1^\dagger on β is shown in figure 20. The curve crosses the zero line at $\beta \approx 0.93$, implying that the upper-branch neutral point of the mode II instability is infinity for $\beta > 0.93$. In the supercritical region, the scaled growth rate $c_{1,i}^\dagger$ increases with β like σ^{-1} , which can be predicted by asymptotic analysis of the low-concentration regime by taking $W_1 \rightarrow \infty$. (The mathematical description is the same as that of the regular-concentration regime, so is omitted here.)

REFERENCES

- BIRD, R., CURTISS, C., ARMSTRONG, R. & HASSAGER, O. 1987 *Dynamics of Polymeric Liquids, Volume 2: Kinetic Theory*. Wiley.
- BUZA, G., PAGE, J. & KERSWELL, R.R. 2021 Weakly nonlinear analysis of the viscoelastic instability in channel flow for finite and vanishing Reynolds numbers. arXiv:2017.06191v1.
- CHANDRA, B., SHANKAR, V. & DAS, D. 2018 Onset of transition in the flow of polymer solutions through microtubes. *J. Fluid Mech.* **844**, 1052–1083.
- CHAUDHARY, I., GARG, P., SUBRAMANIAN, G. & SHANKAR, V. 2021 Linear instability of viscoelastic pipe flow. *J. Fluid Mech.* **908**, A11.
- CHOUËIRI, G.H., LOPEZ, J.M. & HOF, B. 2018 Exceeding the asymptotic limit of polymer drag reduction. *Phys. Rev. Lett.* **120**, 124501.
- CHOUËIRI, G.H., LOPEZ, J.M., VARSHNEY, A., SANKAR, S. & HOF, B. 2021 Experimental observation of the origin and structure of elasto-inertial turbulence. *Proc. Natl Acad. Sci. USA* **118**, 1–5.
- DONG, M., LIU, Y. & WU, X. 2020 Receptivity of inviscid modes in supersonic boundary layers due to scattering of freestream sound by wall roughness. *J. Fluid Mech.* **896**, A23.
- DONG, M. & WU, X. 2013 On continuous spectra of the Orr–Sommerfeld/Squire equations and entrainment of free-stream vortical disturbances. *J. Fluid Mech.* **732**, 616–659.

- DRAZIN, P.G. & REID, W.H. 2004 *Hydrodynamic Stability (Cambridge Mathematical Library)*. Cambridge University Press.
- DUBIEF, Y., PAGE, J., KERSWELL, R.R., TERRAPON, V.E. & STEINBERG, V. 2021 A first coherent structure in elasto-inertial turbulence. arXiv:2006.06770v2.
- DUBIEF, Y., TERRAPON, V.E. & SORIA, J. 2013 On the mechanism of elasto-inertial turbulence. *Phys. Fluids* **25** (11), 110817–110817.
- GARG, P., CHAUDHARY, I., KHALID, M., SHANKAR, V. & SUBRAMANIAN, G. 2018 Viscoelastic pipe flow is linearly unstable. *Phys. Rev. Lett.* **121**, 024502.
- GOLDSTEIN, M.E. 1985 Scattering of acoustic waves into Tollmien–Schlichting waves by small streamwise variations in surface geometry. *J. Fluid Mech.* **154**, 509–530.
- GRAHAM, M.D. 2014 Drag reduction and the dynamics of turbulence in simple and complex fluids. *Phys. Fluids* **26** (10), 101301.
- GROISMAN, A. & STEINBERG, V. 2000 Elastic turbulence in a polymer solution flow. *Nature* **405** (6782), 53–55.
- HAMEDUDDIN, I., GAYME, D.F. & ZAKI, T.A. 2019 Perturbative expansions of the conformation tensor in viscoelastic flows. *J. Fluid Mech.* **858**, 377–406.
- HAMEDUDDIN, I., MENEVEAU, C., ZAKI, T.A. & GAYME, D.F. 2018 Geometric decomposition of the conformation tensor in viscoelastic turbulence. *J. Fluid Mech.* **842**, 395–427.
- KUPFERMAN, R. 2005 On the linear stability of plane Couette flow for an Oldroyd-B fluid and its numerical approximation. *J. Non-Newtonian Fluid Mech.* **127** (2), 169–190.
- LIN, C.C. 1946 On the stability of two-dimensional parallel flows. Part III. Stability in a viscous fluid. *Q. Appl. Maths* **3**, 277–301.
- LIU, Y., DONG, M. & WU, X. 2020 Generation of first Mack modes in supersonic boundary layers by slow acoustic waves interacting with streamwise isolated wall roughness. *J. Fluid Mech.* **888**, A10.
- LOPEZ, J.M., CHOUËIRI, G.H. & HOF, B. 2019 Dynamics of viscoelastic pipe flow at low Reynolds numbers in the maximum drag reduction limit. *J. Fluid Mech.* **874**, 699–719.
- MACK, L.M. 1976 A numerical study of the temporal eigenvalue spectrum of the Blasius boundary layer. *J. Fluid Mech.* **73**, 497–520.
- MESEGUER, Á. & TREFETHEN, L.N. 2003 Linearized pipe flow to Reynolds number 107. *J. Comput. Phys.* **186** (1), 178–197.
- MOHSENI, K. & COLONIUS, T. 2000 Numerical treatment of polar coordinate singularities. *J. Comput. Phys.* **157** (2), 787–795.
- PAGE, J., DUBIEF, Y. & KERSWELL, R.R. 2020 Exact traveling wave solutions in viscoelastic channel flow. *Phys. Rev. Lett.* **125**, 154501.
- RAM, A. & TAMIR, A. 1964 Structural turbulence in polymer solutions. *J. Appl. Polym. Sci.* **8** (6), 2751–2762.
- SAMANTA, D., DUBIEF, Y., HOLZNER, M., SCHÄFER, C., MOROZOV, A.N., WAGNER, C. & HOF, B. 2013 Elasto-inertial turbulence. *Proc. Natl Acad. Sci. USA* **110** (26), 10557–10562.
- SHAQFEH, E.S.G. 1996 Purely elastic instabilities in viscometric flows. *Annu. Rev. Fluid Mech.* **28** (1), 129–185.
- SHEKAR, A., MCMULLEN, R.M., MCKEON, B.J. & GRAHAM, M.D. 2021 Tollmien–Schlichting route to elastoinertial turbulence in channel flow. *Phys. Rev. Fluids* **6**, 093301.
- SHEKAR, A., MCMULLEN, R.M., WANG, S.N., MCKEON, B.J. & GRAHAM, M.D. 2019 Critical-layer structures and mechanisms in elastoinertial turbulence. *Phys. Rev. Lett.* **122**, 124503.
- SID, S., TERRAPON, V.E. & DUBIEF, Y. 2018 Two-dimensional dynamics of elasto-inertial turbulence and its role in polymer drag reduction. *Phys. Rev. Fluids* **3**, 011301.
- SMITH, S. 1979 On the non-parallel flow stability of the Blasius boundary layer. *Proc. R. Soc. Lond. A* **366**, 91–109.
- SMITH, F. 1981 The upper branch stability of the Blasius boundary layer, including non-parallel flow effects. *Proc. R. Soc. Lond. A* **375**, 65–92.
- SURESHKUMAR, R. & BERIS, A.N. 1995 Effect of artificial stress diffusivity on the stability of numerical calculations and the flow dynamics of time-dependent viscoelastic flows. *J. Non-Newtonian Fluid Mech.* **60** (1), 53–80.
- TERRAPON, V.E., DUBIEF, Y. & SORIA, J. 2014 On the role of pressure in elasto-inertial turbulence. *J. Turbul.* **16**, 26–43.
- TREFETHEN, L. 2000 *Spectral Methods in MATLAB*. Society for Industrial and Applied Mathematics.
- VIRK, P.S. 1975 Drag reduction fundamentals. *AIChE J.* **21** (4), 625–656.
- WAN, D., SUN, G. & ZHANG, M. 2021 Subcritical and supercritical bifurcations in axisymmetric viscoelastic pipe flows. *J. Fluid Mech.* **929**, A16.

Asymptotic study of instability in a viscoelastic pipe

- WHITE, C.M. & MUNGAL, M.G. 2008 Mechanics and prediction of turbulent drag reduction with polymer additives. *Annu. Rev. Fluid Mech.* **40** (1), 235–256.
- WU, X. & DONG, M. 2016 Entrainment of short-wavelength free-stream vortical disturbances in compressible and incompressible boundary layers. *J. Fluid Mech.* **797**, 683–782.
- XI, L. & GRAHAM, M.D. 2010a Active and hibernating turbulence in minimal channel flow of Newtonian and polymeric fluids. *Phys. Rev. Lett.* **104**, 218301.
- XI, L. & GRAHAM, M.D. 2010b Turbulent drag reduction and multistage transitions in viscoelastic minimal flow units. *J. Fluid Mech.* **647**, 421–452.
- ZHANG, M. 2021 Energy growth in viscoelastic pipe flows. *J. Non-Newtonian Fluid Mech.* **294**, 104581.
- ZHANG, M., LASHGARI, I., ZAKI, T. & BRANDT, L. 2013 Linear stability analysis of channel flow of viscoelastic Oldroyd-B and FENE-P fluids. *J. Fluid Mech.* **737**, 279–279.
- ZHU, L. & XI, L. 2021 Nonasymptotic elastoinertial turbulence for asymptotic drag reduction. *Phys. Rev. Fluids* **6**, 014601.